

# TERASENSE: THz Device Technology Laboratory

A. García-Pino<sup>(3)</sup>, J. Gutiérrez<sup>(1)</sup>, J. Montero-de-Paz<sup>(8)</sup>, J. Parrón<sup>(6)</sup>, J. Romeu<sup>(2)</sup>,  
R. Vera-Rodríguez<sup>(7)</sup>, P. de Paco<sup>(6)</sup>, L. E. García-Muñoz<sup>(8)</sup>, B. González-Valdés<sup>(3)(5)</sup>,  
M. Moreno-Moreno<sup>(7)</sup>, E. Nova<sup>(2)</sup>, K. Zeljami<sup>(1)</sup>, A. Badolato<sup>(4)</sup>, J.L. Besada<sup>(4)</sup>, T. Fernández<sup>(1)</sup>,  
J. Fierrez<sup>(7)</sup>, J. Grajal<sup>(4)</sup>, G. Junkin<sup>(6)</sup>, J. Marín<sup>(6)</sup>, B. Mencía<sup>(4)</sup>, O. Menéndez<sup>(6)</sup>, J. Ortega-García<sup>(7)</sup>,  
J.P. Pascual<sup>(1)</sup>, O. Rubiños-López<sup>(3)</sup>, D. Segovia-Vargas<sup>(8)</sup>, A. Tazón<sup>(1)</sup>

<sup>(1)</sup> Dpto. Ingeniería de Comunicaciones. Edificio Ingeniería de Telecomunicación, Profesor José Luis García García. Plaza de la Ciencia, S/N. 39005. Santander. Universidad de Cantabria (UNICAN). Spain. [jessica.gutierrez@unican.es](mailto:jessica.gutierrez@unican.es)

<sup>(2)</sup> Dpt. Signal Theory and Communications. Universitat Politècnica de Catalunya (UPC)

Jordi Girona 1-3, 08034 Barcelona. Spain - [romeu@tsc.upc.edu](mailto:romeu@tsc.upc.edu)

<sup>(3)</sup> Depto. de Teoría de la Señal y Comunicaciones, Univ. de Vigo (UVIGO).

ETS Ingenieros de Telecomunicación. Campus Universitario 36310 Vigo. Spain - [oscar@com.uvigo.es](mailto:oscar@com.uvigo.es)

<sup>(4)</sup> Departamento de Señales, Sistemas y Radiocomunicaciones, Univ. Politécnica de Madrid (UPM).

E.T.S.I. Telecomunicación. Ciudad Universitaria 28040 Madrid. Spain - [jesus@gmr.ssr.upm.es](mailto:jesus@gmr.ssr.upm.es)

<sup>(5)</sup> Northeastern University of Boston. 360 Huntington Ave Boston, MA 02115, United States

<sup>(6)</sup> Departament de Telecomunicació i d'Enginyeria de Sistemes. Universitat Autònoma de Barcelona (UAB)

Edifici Q, Campus de la UAB, 08193 Bellaterra (Barcelona). Spain - [josep.parron@uab.es](mailto:josep.parron@uab.es)

<sup>(7)</sup> Biometric Recognition Group - ATVS, Escuela Politécnica Superior, Universidad Autónoma de Madrid (UAM), Avda.

Francisco Tomas y Valiente, 11 - Campus de Cantoblanco - 28049 Madrid. Spain - [ruben.vera@uam.es](mailto:ruben.vera@uam.es)

<sup>(8)</sup> Departamento Teoría Señal y Comunicaciones, Universidad Carlos III de Madrid (UC3M), Avda. Universidad 30,

28911, Leganés. Spain - [dani@tsc.uc3m.es](mailto:dani@tsc.uc3m.es)

**Abstract-** The use of THz frequencies, particularly W and G band allows reaching higher resolution and deeper penetration in emerging applications like imaging, sensing, etc.

The development of those new applications lays on reliable technologies, background of expertise and know-how. The CDS2008-00068 TERASENSE CONSOLIDER project has given the opportunity to extent upwards in frequency the previous background of the microwaves research group partners. This article summarizes the developments of the TERASENSE work package “THz Device Technology Laboratory”.

## I. INTRODUCCIÓN

This paper compiles the developments and activities of the workpackage called “THz Device Technology Laboratory” of the TERASENSE project in the frame of the CONSOLIDER program. The objective of this workpackage was the development of technological activities, up to THz frequencies [1],[2] covering generic technologies for active devices and passive circuits, extraction of models of new devices from DC-RF measurements, design and characterization of devices, MMICs and subsystems. All, keeping in mind that the final applications of these technologies are mainly imaging and sensing systems, which require additionally technologies for data processing [3]-[8].

The interest of the scientific community and the industry in the development of systems working in the W-band atmospheric window is increasing. In the remote sensing area millimeter waves (mmW) offer a good tradeoff between spatial resolution (using relatively small antenna apertures) and material penetration [9],[10]. Moreover, the large available bandwidth and the small system wavelength allow the development of compact wireless high speed communications systems.

The added value of emerging applications in THz bands is divided in different stages starting from the basic active devices and ending with the data processing software. Unfortunately there is a lack of basic active devices (diodes and transistors) manufactured in Spain, and very limited in Europe but there are opportunities for innovation in antenna manufacturing, in design and assembling of circuits and systems and in data processing software.

The antenna design at these frequencies represents a challenge due to the small tolerances required in the construction. Furthermore, the aforementioned mmW applications usually employ electrically large antenna apertures, requiring tens of meters between the antenna under test (AUT) and the probe antenna for the radiation pattern measurement. Therefore, performing far-field (FF) measurements to retrieve the radiation pattern is not feasible unless a compact range measurement system is used. Measuring the antenna gain with a calibrated probe in the FF represents the same problem.

About the available devices and technologies, characterization, modeling and simulation of passive and active devices becomes much more critical to succeed than in microwave circuits and demands intensive use of tools for simulation of active devices and passive structures (with 2D and 3D EM simulators). The accurate knowledge of the properties of dielectric materials, such as those used to manufacture substrates, radomes, or lens antennas, is essential to carry out the design of devices and circuits in the mentioned frequency range. Taking into account the previous experience of the research groups, the design and characterization of circuits operating in these frequencies involved a scale reduction in dimensions, compared to previous expertise in mm-wave circuits, below the limits of previous minimum resolution for printed microstrip/coplanar

circuits and mechanical tolerances in tooling. The upgrade of measurement equipment involved not only the acquisition of new apparatus, but also the change to new connectivity standards.

One of the emerging applications of the millimeter-wave imaging technology is its use in biometric recognition. This is mainly due to some properties of the millimeter-waves such as their ability to penetrate through clothing and other occlusions, their low obtrusiveness when collecting the image and the fact that they are harmless to health. This is in contrast to biometric traits acquired in the visible spectrum, which are normally affected by, among other factors, lighting conditions and occlusions (e.g., clothing, make up, hair, etc.). Section VII describes a biometric recognition system which uses body images acquired at 94 GHz.

Therefore a jump to THz frequencies meant a challenge in all the aspects: modeling, simulation designing, assembling, measurement, etc... The project TeraSense has given the opportunity to extent upwards in frequency the huge background of the microwaves research group partners.

This article will focus on the development of technology aspects by the TeraSense partners: antenna manufacturing, characterization of active and passive devices, design and assembling of circuits and data processing.

## II. ANTENNA MANUFACTURING

All referred THz applications require, as input element, an antenna, whose performance becomes critical for the system but employing a normally affordable technology. Different developments of antennas have been done in the frame of TeraSense.

### A. Linear Patch Antenna Array excited by Slot

A linear array based on three patch antennas excited by slots in W band, has been designed and presented in [11]. The objective has been to obtain an antenna with high directivity, a gain about 13 dBi and a -10 dB bandwidth of 5 GHz, centered at 97 GHz. This task has been developed by UNICAN.

For this goal, initially, a single radiant patch has been designed and optimized its dimensions, obtaining suitable gain and matching, taking each patch formed by a radiant element patch ( $1 \times 1.1\text{mm}$ ) and a slot ( $0.7 \times 0.09\text{mm}$ ). It is obtained a -10 dB bandwidth of 4 GHz at 96 GHz and a directivity of 9.38 dBi with a remarkable backward radiation due to the absence of a below metallic plane.

After validating simulation results of this single patch, two more identical patches were introduced obtaining a good matching and gain, with weak back radiation. The phase center length between patches is 2.2mm and each patch is fed by 100  $\Omega$  microstrip lines (length = 3.7 mm and width = 0.09 mm) and feed lines are connected each other to a 50  $\Omega$  microstrip line (width = 0.26 mm) which, at a distance of 0.5 mm, is enclosed in a cut-off waveguide (dimensions 1.14 mm  $\times$  0.55 mm), in order to propagate only the Quasi-TEM microstrip mode in W-band, from 75 up to 110 GHz. Furthermore, the distance from the feed line to the bottom of the case is 0.5 mm.

The structure of the array has three dielectric layers with their respective metallization. The deeper layer uses the low cost Rogers ULTRALAM 2000 substrate ( $\epsilon_r = 2.5$ ,  $\text{tg}\delta =$

0.0019 and a copper thickness of 18  $\mu\text{m}$ ) with a dielectric thickness of 4 mils to avoid unwanted higher modes propagation. This layer contains the 100  $\Omega$  feed line located at its rear face and the ground plane where the slots are settled at the top face of the same layer. The intermediate layer is the radiant substrate, air in this case, with a thickness of 5 mils. Finally, the top layer which uses Rogers RT/Duroid 5880 with a dielectric thickness of 5 mils ( $\epsilon_r = 2.2$  and  $\text{tg}\delta = 0.0009$ ), holds the metallic patches in its bottom face and acts as a radome.

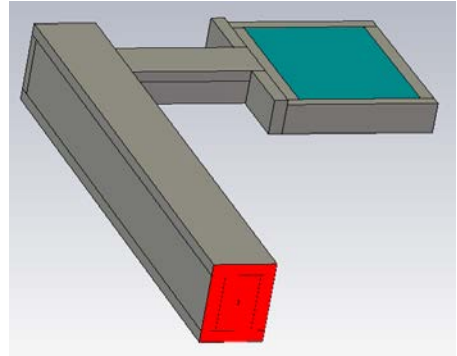


Fig. 1. Patch antenna array with the waveguide-to-microstrip transition

A PNA-X Microwave Network Analyzer with auxiliary Millimeter Wave VNA Extenders in the input and output ports, which present WR-10 waveguide inputs, is used. Therefore, a waveguide-to-microstrip transition, which matches the 50  $\Omega$ -microstrip input impedance of the antenna array structure to the WR-10 waveguide (input of the VNA Extenders), has been necessary to include it in the design to make a more realistic version of the structure. This design it is shown in subsection VI.A.

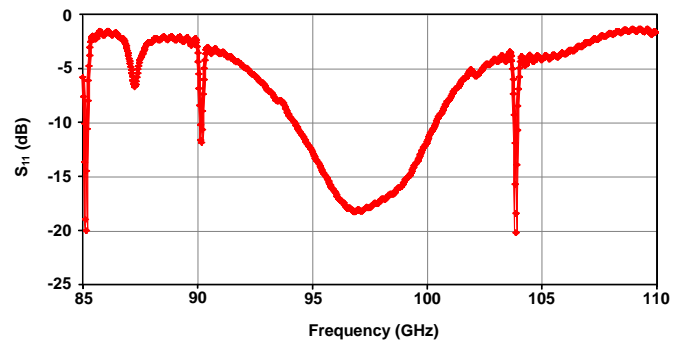


Fig. 2. Matching of the Complete Radiant System

Finally, the complete design composed of the linear array and the waveguide-to-microstrip transition (see Fig. 1) has been evaluated showing no degradation of the array behavior.

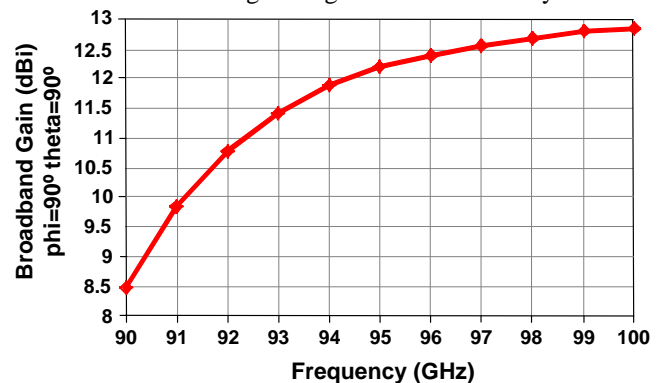


Fig. 3. Gain of the Complete Radiant Structure

The matching of the linear array shown in Fig. 2 presents a -10 dB bandwidth over 5 GHz centered approximately at 97 GHz with suitable phase behaviour. It can be observed that the undesired resonances are out of the interest band of frequencies.

The antenna gain is plotted in Fig. 3, obtaining a good value around of 12.5 dBi at 97 GHz, according to the number of patch elements of the array.

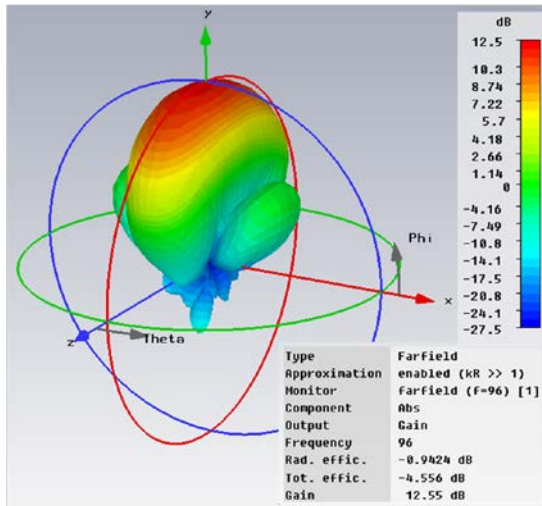


Fig. 4. Pattern Radiation of the Complete Radiant Structure

Finally, in Fig. 4, the 3D pattern radiation of the complete radiant system at 96 GHz it is shown. It can be seen a gain of 12.55 dBi with backward radiation of -25 dB Main Lobe Level and a -14 dBi Side Lobe Level, typical value in this type of structure.

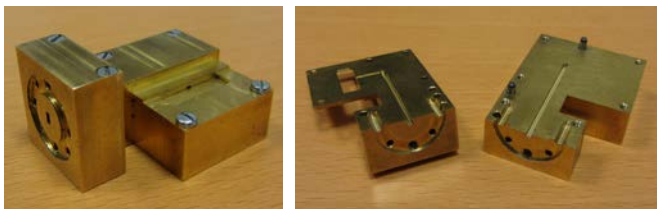


Fig. 5. Photographs of the metal case for the patch antenna array

The antenna prototype has been made up in two stages: the metal case and the radiant elements [12]. On the one hand, the entire metal case has been split in two pieces (see Fig. 5). The suitable cutting plane has been located in order to contain the entire cutoff cavity in one half avoiding undesired resonances due to possible defects. The final dimensions of the metal case are 4 × 3 cm.

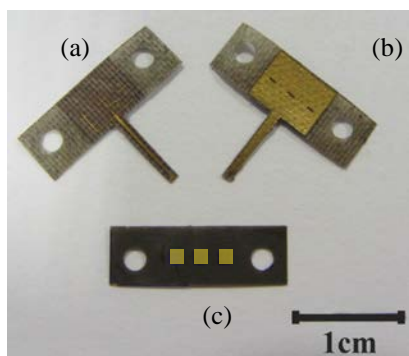


Fig. 6. Photographs of the microstrip lines for the complete radiant system. (a) feed lines and microstrip lines of the waveguide-to-microwave transitions, (b) slots and (b) three array patches

On the other hand, the feed lines have been obtained following the procedure introduced in section II. In Fig. 6, it can be seen the layers that constitute the complete radiant system.

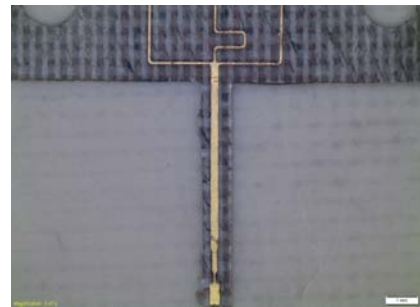


Fig. 7. Zoom of the deeper layer of the complete radiant system

The feed lines of the antenna can be seen in Fig. 7 wherein a zoom of the deeper layer is displayed.

The system will be assembled in order to obtain experimental results.

### B. 94 GHz Cassegrain Reflector Antenna

This section presents a solution to overcome the limitations mentioned above in the design and measurement of electrically large antennas at mmW [13]. This task has been developed by UPC. The radiation pattern results obtained with a NF to FF transformation technique are shown in section B.1. Moreover, the efficiency has been measured using a radiometric technique to obtain the gain pattern. Finally, the tolerance effects in the RL for several antenna prototypes are exposed in section B.2 and a waveguide matching network is proposed to match the antenna impedance at 94 GHz.

The measurements results correspond to a 94 GHz cassegrain antenna with a main reflector of 160 mm diameter. Fig. 8 shows a photograph of the antenna describing its most relevant parts. The feeder consists on a horn antenna with a Teflon top in order to have a watertight structure.

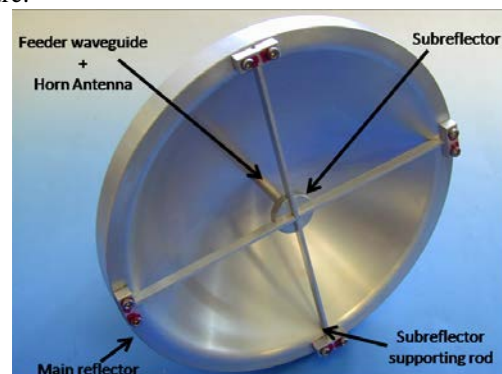


Fig. 8. Photograph of the antenna under test

#### B.1 Radiation pattern measurement

The radiation pattern of the antenna has been obtained by transforming the measured electric field of the antenna aperture. The electrical field has been sampled each  $0.45\lambda$ , obtaining a matrix of 140x140 electric field values corresponding to an area of 201x201 mm at 5 cm from the reflector aperture.

Fig. 9 shows a photograph of the 2D NF measurement setup. It is composed by a W-band network analyzer with a transmitter header connected to the AUT and fixed to an

optical table. The probe is connected to the receiver and held on a 2D scanner with 300x300 mm travel. An RF absorber has been used to avoid reflections from the scanner and the receiver header.

The radiation pattern has been measured after the antenna construction, after a thermal shock test and after vibration test. Fig. 10 shows the results of the E-plane, H-plane and a 45° cut of the radiation pattern measured before and after the environmental tests. It should be pointed out that the variation of the results after the environmental tests are negligible.

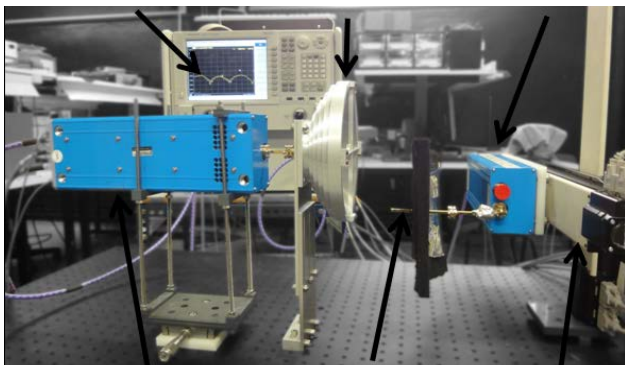


Fig. 9. W-band near field scanning setup

Several radiation parameters are extracted from the radiation patterns: a directivity of 41.3 dB, a -3dB beam width  $\Delta\theta_{-3dB}$  of 1.42°, a E-plane side lobe level of 21.7 dB and a H-plane side lobe level of 22.9 dB.

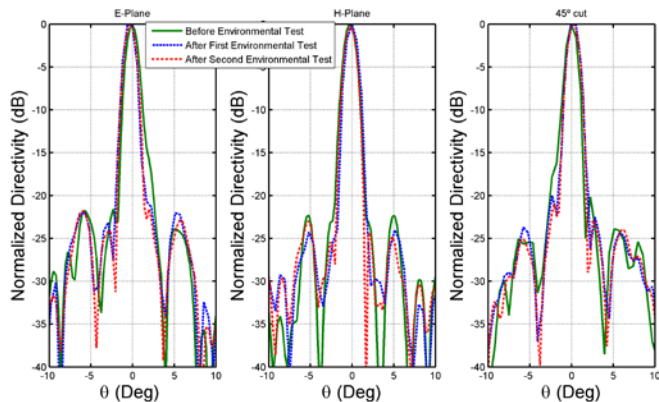


Fig. 10. Measured radiation patterns of the cassegrain antenna after construction and after two environmental tests

### B.2 Antenna efficiency measurement

The antenna efficiency has been measured using a radiometric technique. Fig. 11 shows the total power radiometer components. The local oscillator frequency is at 94 GHz and the baseband signal is filtered at 400 MHz. Therefore the antenna losses are averaged from 93.6 to 94.4 GHz. A horn antenna has been used as a reference antenna (supposing no losses) in order to calibrate the radiometer looking to the sky using a calibrated attenuator. As a result 2.9 dB of losses have been obtained in the antenna, giving an antenna gain of 38.3 dB.

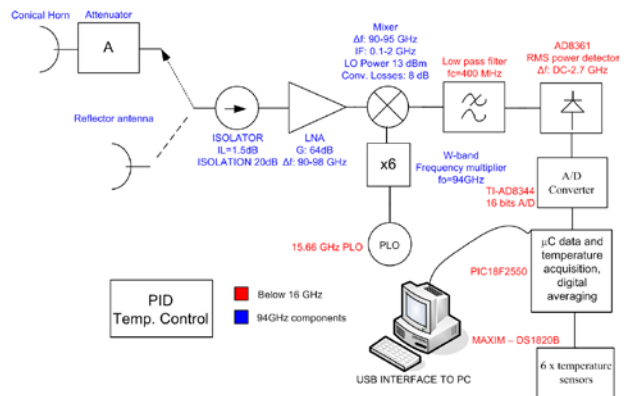


Fig. 11. Radiometer hardware components schematic

Due to the tolerances in the Teflon cap construction, the RL of the antenna is not matched at 94 GHz. Fig. 12 shows the variability of the RL for different antenna prototypes. Using a waveguide matching network composed by 3 capacitive screws, all the antennas are matched at 94 GHz with a RL below -18 dB as shown in Fig. 13.

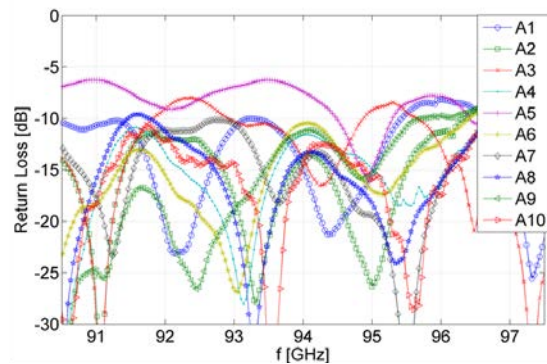


Fig. 12. Return loss of 10 different antenna prototypes before impedance matching

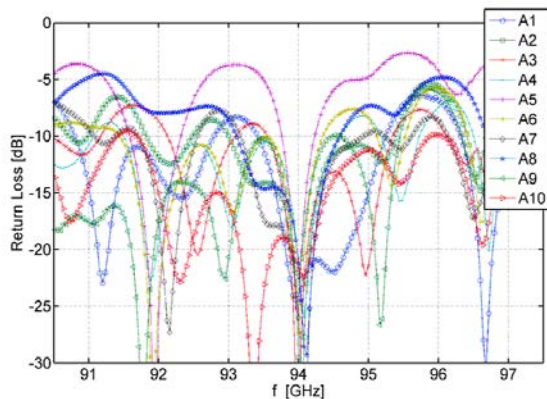


Fig. 13. Return loss of 10 different antenna prototypes after impedance matching

### C. Bifocal Reflector Antenna Prototype for Radar Imaging at 300 GHz

A 300GHz high-resolution imaging system for security applications (such as detection of weapons or concealed contraband on persons) has been developed by GMR-UPM and Antenna-UVigo groups. The system utilizes the CW-LFM (Continuous-Wave Linear-Frequency Modulation) radar technique. Its operational bandwidth goes from 286.2 to 313.2 GHz, within a window of atmospheric attenuation. In such frequencies, a wide range of materials (clothing, paper, plastic, wood ...) is reasonably transmissive.

The radiating system utilizes Bifocal Ellipsoidal Gregorian Reflector geometry with a small mechanical rotating mirror to achieve an image resolution less than 2 cm at a standoff range of 8 m within a scanned area of 0.8 m x 0.5 m. The antenna prototype can be seen in Fig. 14. It is composed of the following elements:

(a-b) The main reflector and the subreflector are shaped surfaces configured as the Bifocal Ellipsoidal Gregorian Reflector System (BEGRS) described in [14], in order to improve the scanning behavior of the antenna, provide higher field of view, increase the antenna gain in the target region and allow better control of the scanning operation. In addition, the subreflector must be oversized in order to span the field of view to the size of the human torso.

(c) In order to provide scanning characteristics, the illuminating wave arrives at the subreflector after being reflected in the mirror. The mirror is flat and lightweight. It has two rotation axes providing two different motions: a fast rotating motion about a primary axis which can be rotated slowly about a secondary axis along (vertical tilting).

(d) A feed reflector designed to illuminate the subreflector with a tapered collimated beam.

(e) A silicon beam splitter to separate the transmitted and received beams.

(f) A transmitting horn whose beam passes through the feed splitter.

(g) A receiving horn taking the reflected beam at the beam splitter.



Fig. 14. 300GHz antenna prototype

#### D. Active Antennas in the W-Band based on Schottky Diodes

This section shows the development of a Schottky Barrier Diode (SBD) based compact receiver module operating in the E-band (71-76 GHz) [15]. This task has been developed by UC3M. In order to achieve a compact receiver, direct envelope detection is used, avoiding the need of a local oscillator (LO) signal. The module is shown in Fig. 15 and it comprises a hyper-hemispherical Si lens, a zero-bias SBD which is mounted on a planar antenna, and a 50Ω low frequency impedance matching output.

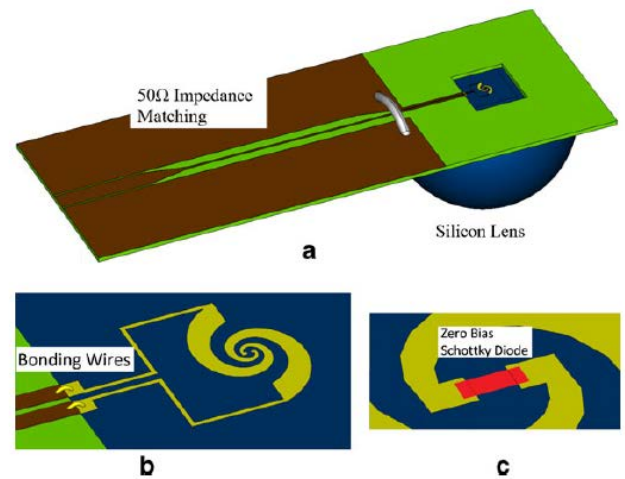


Fig. 15. Schematic of the SBD QO Video Detector with log-spiral antenna. Materials: dark blue part is the silicon lens and silicon substrate where the gold (yellow part) planar antenna is grown, while green part is FR-4 material and brown part is copper. Bonding wires are included to connect gold lines over silicon to copper lines over FR-4 and a metallic wire is inserted to interconnect both ground planes of CPW line. Zero Bias Schottky diode is epoxied in the middle of the antenna. (a) Complete SBD QO Video Detector 3D schematic. (b) Antenna zoom. (c) Schottky diode zoom [15]

#### D.1 Receiver Design

In the design of the antenna, both gain (directivity \* radiation efficiency) as well as matching between antenna and active element (antenna impedance) need to be taken into account [16]. We have designed and fabricated three different planar antenna types: Meander Dipole, Log-Spiral and Log-Periodic, to evaluate which one provides the best performance to the receiver module. Meander dipole has been designed to maximize the power delivered from the antenna to the SBD at the millimetre-wave carrier frequency range, matching the impedance of the antenna to the impedance of the SBD [17]. With Log-Spiral and Log-Periodic antennas a constant broadband response is expected.

#### D.2 Measurements

Three receivers were manufactured and measured within the E-Band. A picture of the Log-Spiral receiver can be seen on Fig. 16.

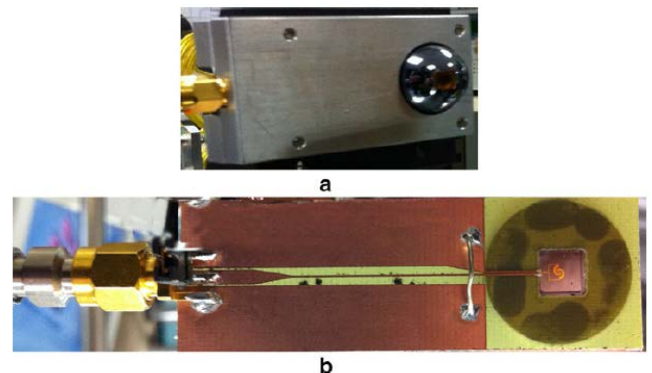


Fig. 16. Photograph of the receiver module: (a) Front view of the cased module showing the Si lens, and (b) Back view of uncased module, showing the Log-Spiral antenna on HR-Si and the impedance matching transition to the SMA output connector [15]

The measured responsivity, as the signal produced by the power arriving to the SBD receiver, is shown on Fig. 17. The effective area normalized peak responsivity of the receiver in the 70-76 GHz band is found to be 814.4 V/W and 740.3 V/W for the Meander Dipole and the Log-Spiral antenna respectively. The module with log-periodic antenna exhibits a responsivity value reaching 1278 V/W at 72GHz.

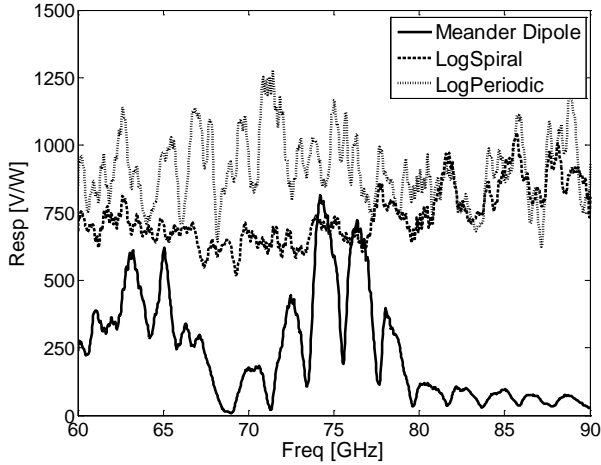


Fig. 17. Responsivity spectra measured over the E-band for the Meander Dipole, Log-Spiral and Log-Periodic antennas [15]

### III. CHARACTERIZATION AND MODELLING OF BASIC ACTIVE DEVICES

As it was previously mentioned, the fabrication of basic active devices (transistors and diodes) to operate in THz bands is nowadays completely out of the scope of the project. It is not possible at all to compete with companies (mainly in USA) with a background of decades and a strong government support in space and military programs.

Luckily, some devices are commercially available, like high performance diodes from Virginia Diodes. Such Diodes may be essential part of detectors, mixers and multipliers.

Those subsystems may be designed and assembled in affordable hybrid technology, but requiring accurate modeling to achieve success.

Schottky diodes are used for design of detectors, mixers and frequency multipliers in sub-millimeter wavelengths. In addition, the planar diode opens up the possibility of diode circuit integration.

In this section an ultra-wideband (DC to 110 GHz) model, for a single Anode Schottky Diode (Virginia Diodes VDI) is presented [18]. This task has been developed by UNICAN. Model extraction is based on different measurements [19] and computer-aided parameter extraction have been performed to obtain a complete large-signal equivalent circuit model suitable for the device under consideration up to 110 GHz, and for its integration in planar circuits. Measurements were: direct current (DC) characteristics, capacitance measurements, scattering (S) parameter measurements and measurements of the assembly of Coplanar to Microstrip bonded transitions used to achieve the complete final diode model up to 110 GHz [20]. In accordance with the availability of measurement equipment, the measurements were carried out in two frequency ranges: DC-50 GHz and 75-110GHz. To verify theoretical models of the Schottky diode, biased

measurements are done to measure the characteristics of the junction capacitance.

#### A. Direct current (DC) characterization of Schottky diodes

A Schottky Diode can be modeled as a combination of resistance and capacitance, both bias-dependent. The Schottky diode model consists of both, linear and nonlinear parts. The nonlinear part corresponds to the metal-semiconductor junction, and the linear part contains everything else. An accurate modeling of parasitic effects introduced by the diode package elements is necessary. Several studies on diode modeling have been done.

A widely recognized model is the thermionic-field emission model generalized I-V characteristics, equation (1), capacitance-voltage relationship, taking into account the dependent junction capacitance, has been given by (equation 2):

$$I(V_d) = I_s \left[ \exp\left(\frac{q(V_d - I_d R_s)}{\eta k T}\right) - 1 \right] \approx I_s \exp\left(\frac{q(V_d - I_d R_s)}{\eta k T}\right) \quad (1)$$

$$C_j(V) = \frac{dQ}{dV} = \frac{C_{j0}}{\left(1 - \frac{V_j}{\phi_{bi}}\right)^\gamma} \quad (2)$$

Fig. 18 shows the measured DC I-V, and C-V data, compared with the model (comparison between on-wafer S-parameter measurements and with low-frequency measurements using a LCR meter) [21]. As can be seen, the model predicts quite well all these measurements.

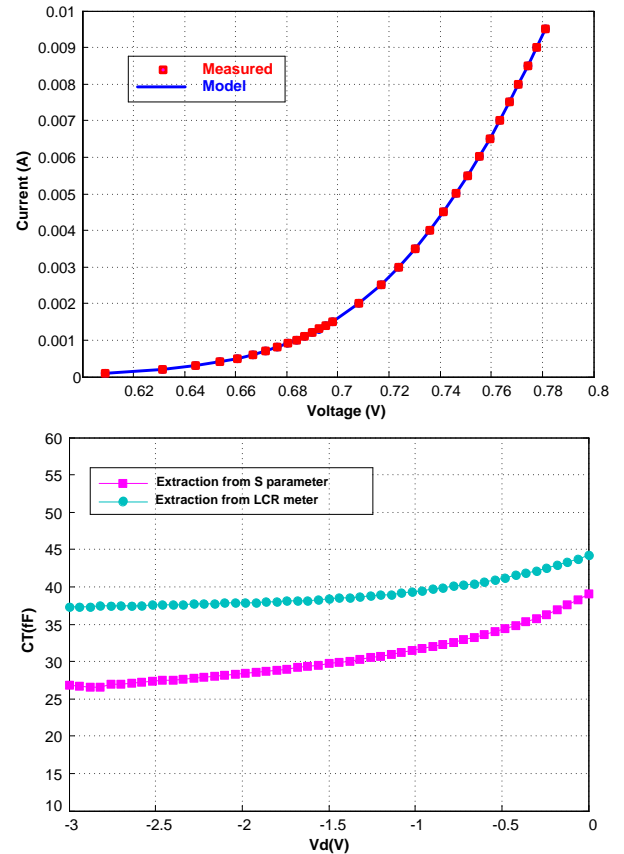


Fig. 18. DC I-V curve, and C-V measurements and simulations

### B. Characterization of diode: simulation (modeling tools)

Voltage dependency of  $C_j(V)$  and  $R_j(V)$  can be implemented using a SDD (Symbolically-Defined-Device) module from ADS. Fig. 19 shows a Single Anode Diode (SA-Diode) under consideration. The nominal overall chip dimensions of the diode are  $600\mu\text{m} \times 250\mu\text{m} \times 100\mu\text{m}$  (length x width x thickness). It is connected with coplanar-to-Microstrip transitions (model PROBE POINT TM0503 JmicroTM transition). This configuration allows enabling on-wafer measurements using air coplanar probes, but in this case requires the use of wire bonding connections.

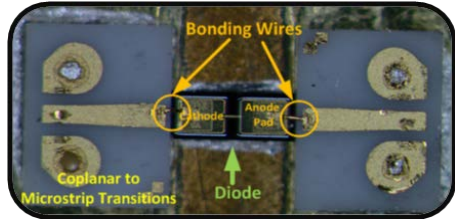


Fig. 19. Single Anode Diode bonded with gold wires (diameter of  $17\mu\text{m}$  and length  $200\mu\text{m}$ - $210\mu\text{m}$  at both sides)

### C- Equivalent circuit model of the diode (lumped elements: intrinsic and extrinsic)

Fig. 20 shows the equivalent circuit proposed for the discrete planar Schottky diode under consideration in order to illustrate its integration in a microstrip circuit environment including bonding wires. The circuit includes a finger inductor  $L_p$  (estimated using the planar inductor approximation) and a pad-to-pad capacitor  $C_{pp}$ . In parallel with the Schottky junction is the finger-to-pad capacitance component  $C_p$ . A set of simple lumped elements models parts inside and outside the diode: an ideal inductance  $L_2$  in series with resistor  $R$  represents the wire inductance and losses due to the metallization and wire bonding, as well as radiation losses at the wire bends. The two shunt capacitances close to the input and output ports ( $C_1$ ,  $C_2$ ) represent the substrate capacitance between the microstrip lines onto which the wire is bonded. The inductor  $L_1$  represents end inductance caused by the wire bonds.

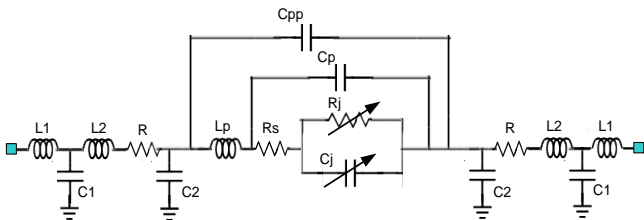


Fig. 20. Lumped equivalent circuit for Schottky diode with the extrinsic elements detailed

The intrinsic device is represented through its characteristic elements:  $R_j$  is the nonlinear Schottky junction resistance that acts in parallel with the diode junction capacitance  $C_j$ , and the ohmic contact resistance is denoted by  $R_s$ . The equivalent values for each intrinsic element component are extracted from measured direct current (DC) characteristics and scattering parameters with fixed RF power levels ( $\leq -30\text{ dBm}$ ), and the diode unbiased and also reverse biased.

### D. Results

S-parameter measurement data are compared with Schottky diode models in Agilent ADS with additional parasitic elements as shown in Fig. 21. The target variables are extracted by performing curve fitting to the measured data. It should be noted here that our model takes into account the increase of the wire bonding series resistance caused by the skin effect at frequencies above 50 GHz and eventually by some other measurement uncertainties. In accordance with the measurement equipment facilities at our laboratories, the measurements were carried out in two frequency ranges: DC-50 GHz and 75-110 GHz [21].

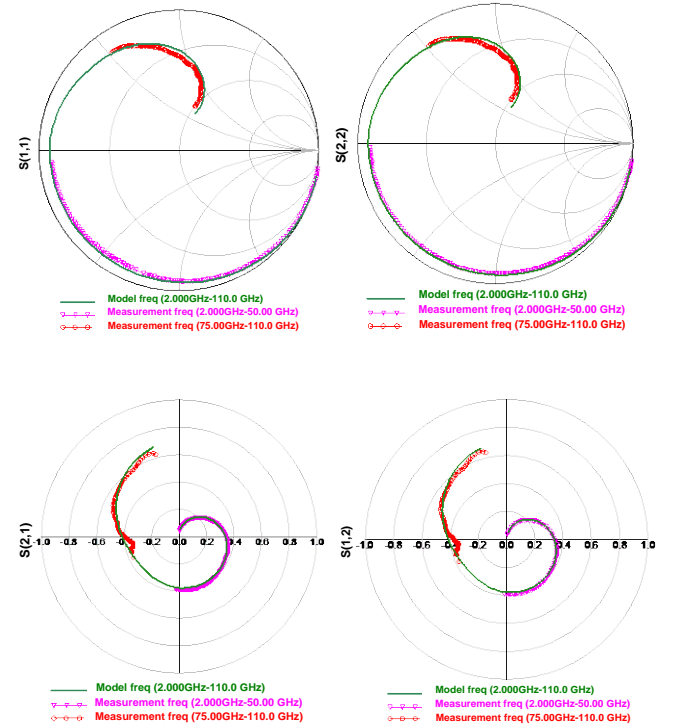


Fig. 21. S-Parameter simulation and measurement for Schottky Diode using diode model (Fig. 20). Diode is unbiased (0V)

Parameters	Symbol	Value
Saturation current(A)	$I_{\text{sat}}$	$9.97593\text{e-}13$
Ideality factor	$\eta$	1.28
$nkT/q$ (1/V)	$\alpha$	30.31
Zero junction capacitance (fF)	$C_{j0}$	24
Series resistance( $\Omega$ )	$R_s$	2.4429
Built in potential (V)	$\Phi_{\text{bi}}$	0.9
Finger inductance (pH)	$L_f$	50
Parasitic Capacitance (fF)	$C_p$	1
Pad-to-pad capacitance (fF)	$C_{\text{pp}}$	15
Bonding Inductance (pH)	$L_1$	60.13
Bonding Inductance (pH)	$L_2$	51.36
Pad capacitance (fF)	$C_1$	60.34
Pad capacitance (fF)	$C_2$	46.26
Bonding resistance ( $\Omega$ )	$R$	0-3

Table 1. Extracted parameters of the Schottky diode under consideration

The capability of our characterization and modeling method has been demonstrated to create a reliable equivalent circuit model of Schottky diodes with very good accuracy and valid under large signal conditions and at high frequencies up

to 110 GHz. This was demonstrated using measurements up to 50 GHz and between 75 GHz and 110 GHz, although with a lack of measurements in the 50-75 GHz range. Using this model, the degree of agreement between measurements and simulations, for different diodes, validated the proposed approach. Simulated performance for the Zero Bias Diode (ZBD) and antiparallel diodes configuration structures provides accurate predictions of the device performance up to 110 GHz. The parameters extracted from zero bias diode provide an accurate RF model for nonlinear circuit simulations to design diode detectors.

#### IV. DESIGN OF MMICS

Some of the partners in TeraSense have a large background in design of MMICs and one of the goals of the project was to extend this experience to THz band, at least in the W band, to be able to provide added value in the MMICs design stage. Moreover, the use of, not Spanish, but at least European foundries was a strategic purpose. The list of foundries open to supply W band technology was very limited (IAF, OMMIC, UMS). Finally a set of MMICs own designed with European technology (OMMIC, France) was developed, but not yet manufactured due to limitations in budget (each prototype costs about 20.000€).

A single stage cascode LNA and a medium power amplifier have been designed with D007IH and D01MH OMMIC technology processes. Also a 4-stage LNA and a single dual balanced mixer are being designed, but they are not yet finished. This task has been developed by UNICAN.

##### A. Cascode Low Noise Amplifier (94-100 GHz)

The complete design of a Cascode Low Noise Amplifier (LNA) MMIC operating in a band between 94 and 100 GHz and based on microstrip technology using a process which employs 0.07  $\mu\text{m}$  Metamorphic High Electron Mobility Transistors (D007IH OMMIC process), has been presented in [22]. A modified Cascode configuration combining resistive feedback and a lossy network to equalize gain and stabilize the circuit is used. The schematic diagram of the LNA is illustrated in Fig. 22, where it can be seen with detail the structure of the design. The size of the transistors used is 4 x 15  $\mu\text{m}$ .

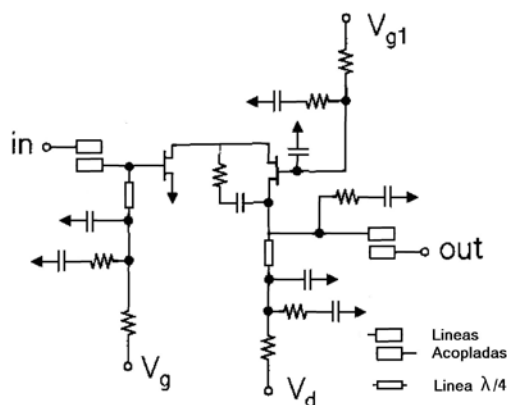


Fig. 22. Schematic Diagram of the LNA

The layout of the final LNA which is prepared to be sent to OMMIC foundry is shown in Fig. 23, where the free space of the dice has been used to place same transistors to be characterized in the future.

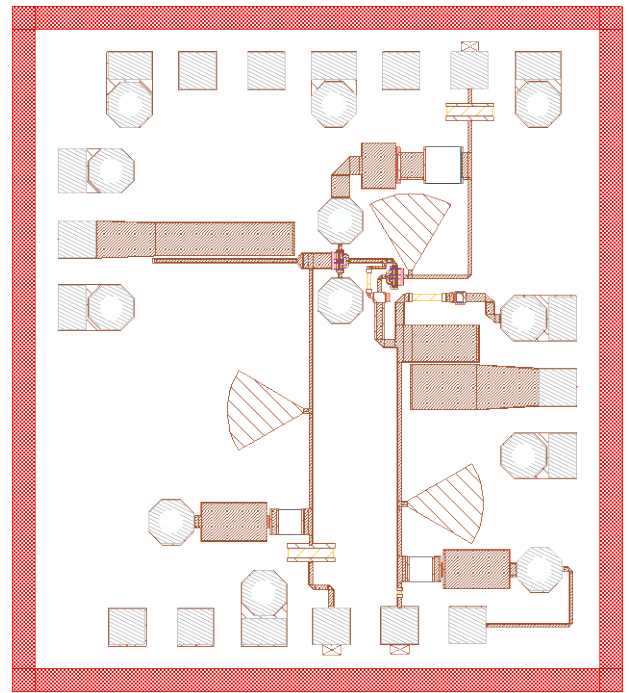
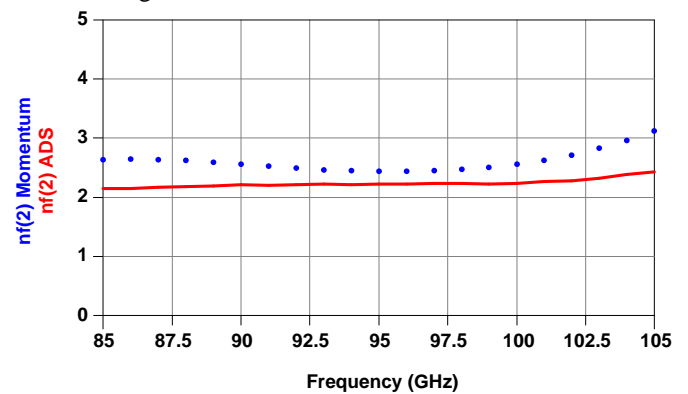


Fig. 23. Layout of the LNA (1.5 x 1.335 mm<sup>2</sup>)

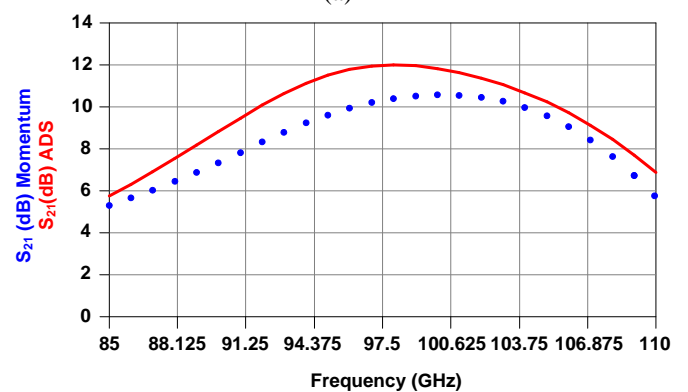
The results obtained with the simulation based on the component models and the results obtained replacing the different passive networks of the design by their own S-parameters simulated in Momentum are presented and compared in Fig. 24, Fig. 25 and Fig. 26.

In Fig. 24, it is shown the small signal gain which is over 11 dB and the Noise Figure (NF) with a minimum value of 2.2 dB, being below 2.5 dB in the whole band.



Frequency (GHz)

(a)



Frequency (GHz)

(b)

Fig. 24. Noise Figure Results and Gain  $S_{21}$  of the Schematic design (solid line) and Momentum (dotted line)

Regarding to the input and output matching,  $S_{11}$  and  $S_{22}$  are better than -15 dB and -8dB in the band of frequencies 94-100 GHz.

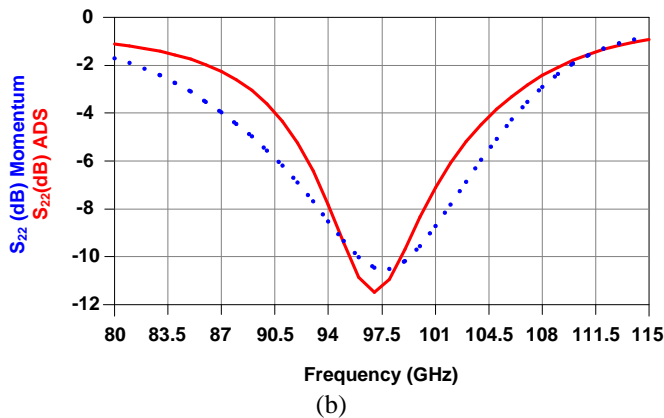
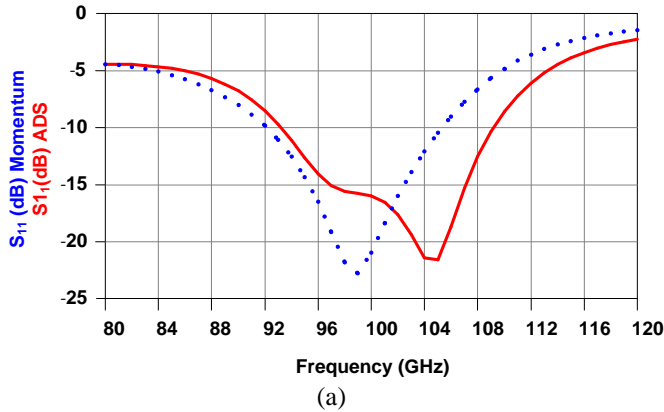


Fig. 25. Input and Output Matching of the LNA simulated in Schematic (solid line) and Momentum (dotted line)

The stability analysis parameter  $\mu$  has a value upper than 1 in the entire band where the model is valid, ensuring the unconditional stability of the LNA (see Fig. 26).

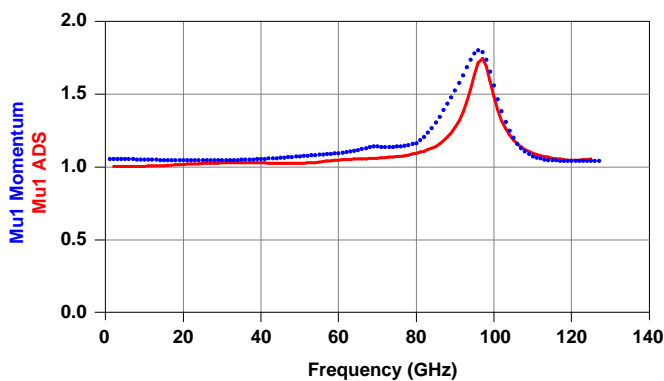


Fig. 26. Stability factor parameter  $\mu > 1$ : unconditional stability for all frequencies

A summary of the principal parameters to take into account for a properly performance of the circuit design is shown in Table 2.

SYMBOL	MIN.	TYP.	MAX.
GAIN (dB)	11.2	11.7	11.9
REFLECTION COEFFICIENTS (dB)	$S_{11}$	-12.8	
	$S_{22}$	-9.7	
NOISE FIGURE (dB)			2.3
INPUT FREQUENCY (GHz)	94		100
VOLTAGE BIAS (V)	$V_{G1}$		-0.1
	$V_D$		3.85
	$V_{G2}$		1.4
$I_{SUPPLY}$ (TOTAL) (mA)		2.2	
$P_{DC}$ (mW)		3.1	

Table 2. Summary of fundamental characteristics of LNA

### B. A Three-Stage Medium Power Amplifier (94-100 GHz)

The design of a three-stage Medium Power Amplifier (MPA) MMIC operating in a band between 94 and 100 GHz has been explained in [23]. The amplifier circuit is based on a microstrip lines design with  $0.13 \mu\text{m}$  gate length Metamorphic High Electron Mobility Transistors (D01MH OMMIC process). The schematic diagram of the LNA is illustrated in Fig. 27, where it can be seen with detail the stages of the design. The size of the transistors used is  $4 \times 20 \mu\text{m}$ .

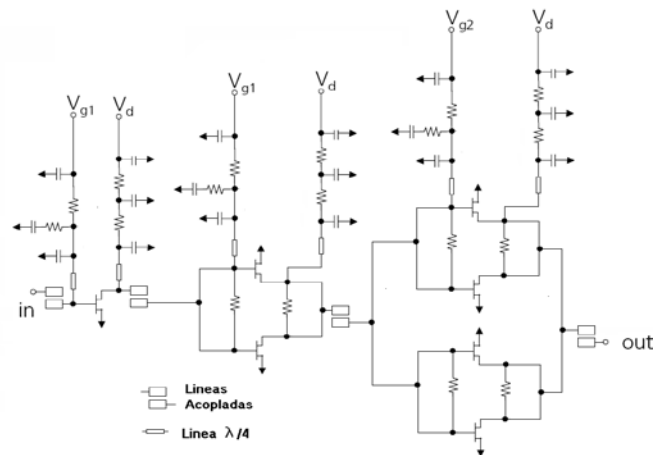


Fig. 27. Schematic Diagram of the MPA

The layout of the final LNA which is prepared to be sent to OMMIC foundry is shown in Fig. 28, where the free space of the dice has been used to place same transistors to be characterized.

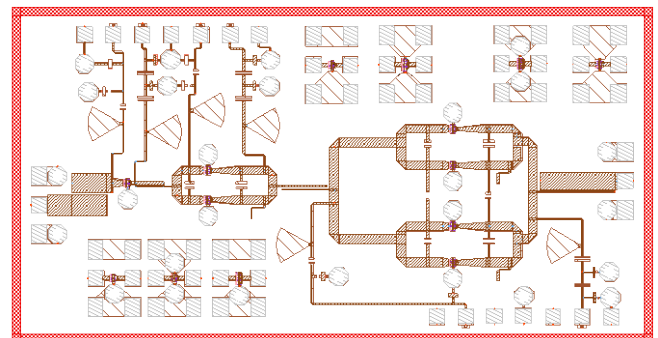


Fig. 28. Layout of the MPA ( $1.743 \times 3.314 \text{ mm}^2$ )

Simulations have been carried out with the non linear complete model of MHEMT transistors to describe their behavior in large signal. DC bias chosen was:  $V_{gs1} = -0.05$  V,  $V_{gs2} = -0.15$  V and  $V_{ds} = 4$  V, obtaining a reasonable gain in spite of limiting the reached efficiency. The Pin-Pout curve has been simulated at a central frequency given in the band, obtaining the gain in available power (see Fig. 29). The 1dB compression point is placed in  $P_{out1dB} = 13.12$  dBm for  $P_{in} = 2.6$  dBm.

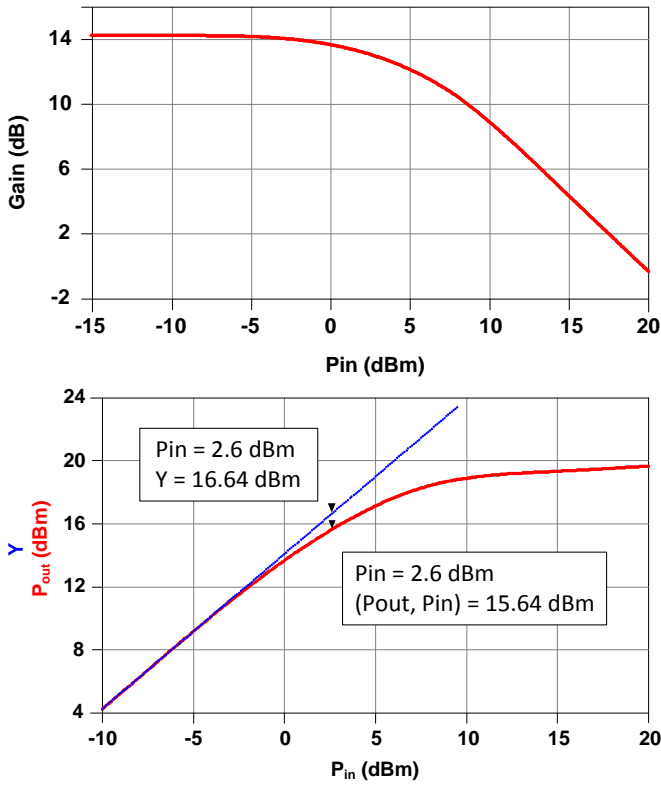


Fig. 29. Gain curve and Pin / Pout at 97 GHz

The Power Added Efficiency (PAE) has been evaluated too, reaching values above 10%. PAE is plotted in Fig. 30.

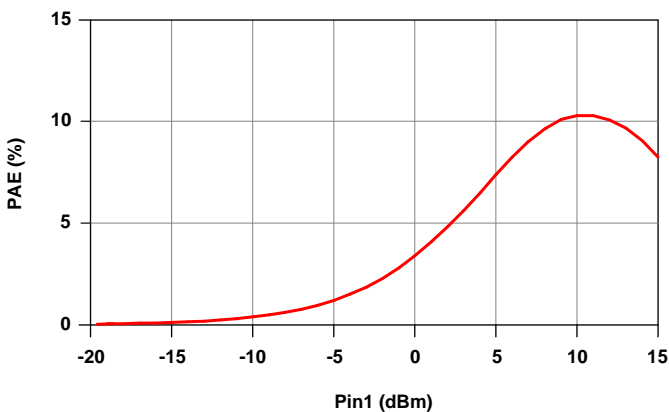


Fig. 30. PAE as a function of  $P_{in}$

The behavior in function of the frequency has been evaluated using large signal S-parameters, which considering the injected power level in the amplifier and let show the compression of the gain. In the Fig. 31, the gain as a function of frequency for a wide range of input power is plotted. It can

be seen the gain curves progressively compressed from 4 dBm of input power.

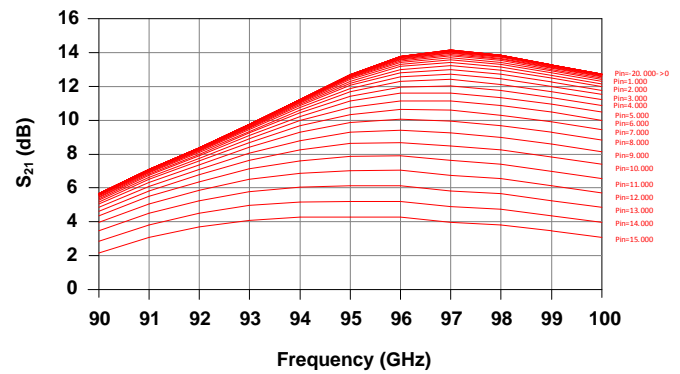


Fig. 31. Gain as a function of frequency varying  $P_{in}$  from (-20 dBm to 15 dBm) using Large-Signal S-parameters analysis

In Fig. 32, the input matching is shown, where the compression can be seen as deterioration of the values, and in Fig. 33, the output matching is shown which is less sensitive to the input power.

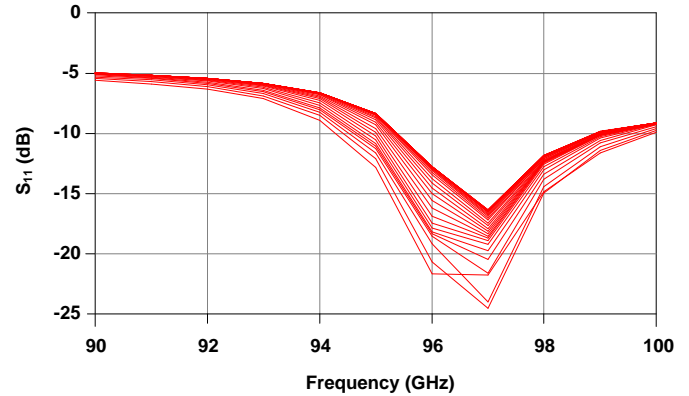


Fig. 32.  $S_{11}$  (dB) in Large Signals function of frequency varying  $P_{in}$  from (-20 dBm to 15 dBm)

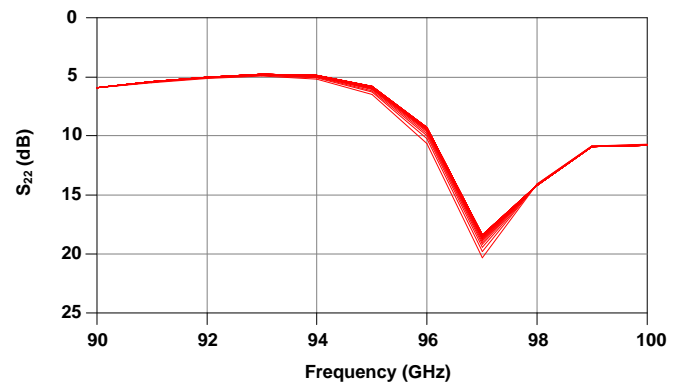


Fig. 33.  $S_{22}$  (dB) in Large Signal function of frequency varying  $P_{in}$  from (-20 dBm to 15 dBm)

A summary of the principal parameters to take into account for a properly performance definition of the designed circuit is shown in Table 3.

SYMBOL		MIN.	TYP.	MAX.
GAIN (dB)		11.25	13.3	14.15
REFLECTION COEFFICIENTS (dB)	$S_{11}$	-7.9		
	$S_{22}$	-4.5		
INPUT FREQUENCY (GHz)		94		100
OUTPUT POWER(1dB) @ 97 GHz (dBm)			15.5	
VOLTAGE BIAS (V)	$V_{G1}$		0	
	$V_D$		3.5	
	$V_{G2}$		0	
	$V_{G3}$		-0.2	
$I_{SUPPLY}$ (TOTAL) (mA)			213.0	
PAE (%)				8.9

Table 3. Summary of fundamental characteristics of MPA

### V. ON WAFER CHARACTERIZATION OF COMMERCIALY AVAILABLE MMICS

There is a very limited list of suitable MMIC circuits commercially available, most of them manufactured in USA and available with restrictions. One of the most interesting suppliers is Hughes Research Labs (HRL) which fabricates W band LNAs with 4 and 5 stages, Medium power amplifiers and detectors.

Those devices could be acquired as a dice or eventually already connectorized. The former option retains some added value but requires facilities, first for measuring and characterization and later for assembling.

This task has been developed by UNICAN. Facilities available for on wafer testing were: Vectorial Network Analyzer in W band (PNAX + W heads) + probe station Cascade Summit+ picoprobe probes 125  $\mu\text{m}$  pitch (Fig. 34).



Fig. 34. Laboratory set-up for on wafer measurements of MMICs

The first measurements of the available MMICs are done on wafer [24] in order to verify the specifications provided by the manufacturer. On the one hand, the 5-stages LNA (LN5-100) with its DC biasing network formed by different values of capacitors and resistances (10 $\Omega$  for drain and 1K $\Omega$  for gates) is shown in Fig. 35.



Fig. 35. LN5-100 on wafer assembly

The four S-parameters measured are shown in Fig. 36. A constant gain from 75 up to 102 GHz (working range of this LNA) with a maximum value about 16 dB (below the desired value of 29 dB which is the provided gain by the manufacturer) has been measured. This can be due to an unwanted oscillation or a possible damaged stage.

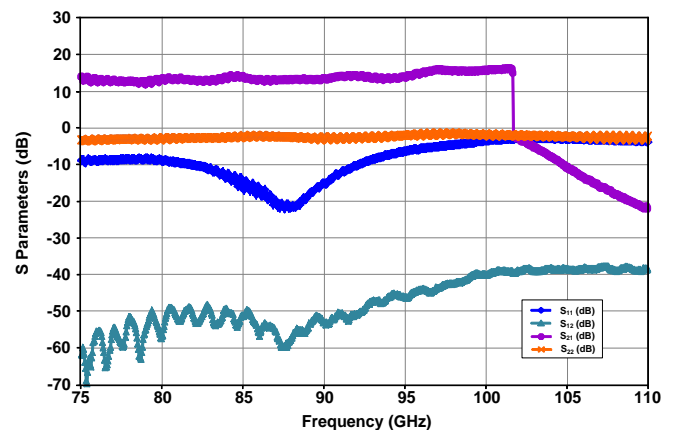


Fig. 36. S-parameters measured of LN5-100 (HRL)

On the other hand, the 4-stage LNA (LN4-110) shown in Fig. 37 has been assembled with the same type of biasing networks as the previous LNA and the S-parameters measured are shown in Fig. 38.

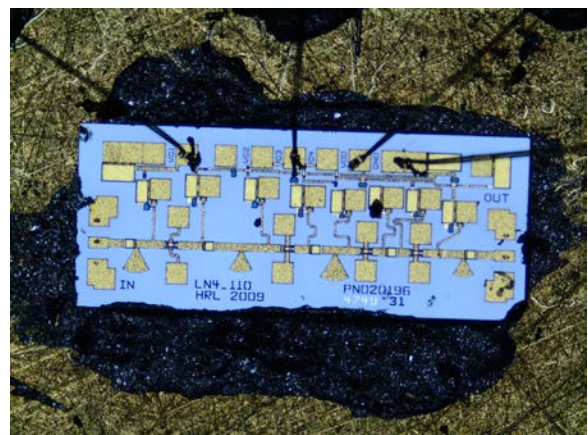


Fig. 37. LN4-110 on wafer assembly

In this LNA, the gain has a constant behavior in the entire range, but in this case, with a maximum value around 20 dB, higher than the LN5-100 gain and much more similar to the expected response (24 dB is the value given by the manufacturer). Furthermore, this LNA operates in the entire W band (from 75 up to 110 GHz), therefore LN4-110 has been chosen for the future radiometer because seems more stable and reliable than the 5-stage LNA. If it were necessary to obtain a higher sensitivity with a suitable level of gain, it could be possible to cascade two LN4-110.

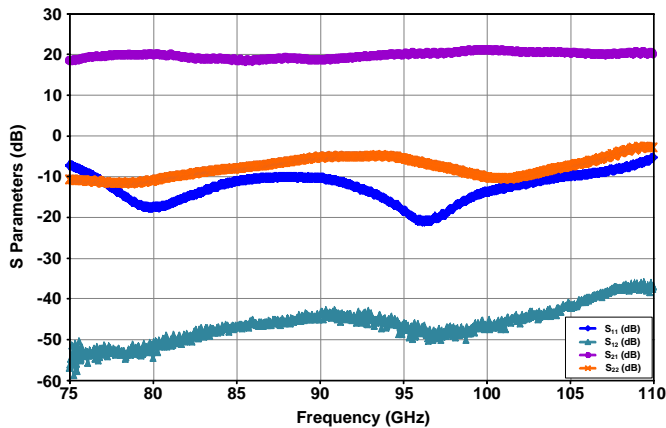


Fig. 38.S-Parameters measured of LN4-110 (HRL)

Noise figure indicated by manufacturer (NF=3dB for LNA5 and NF=3.5dB for LNA4) could not be confirmed due to the lack of noise figure measurement facilities in W band.

The diode-detector V1A MMIC presents a high sensitivity given by the manufacturer about 15.000 mV/mW at 95 GHz. The laboratory set-up has been the same for the LNAs measurements using the PNA-X and the probe station with picoprobe probes 125  $\mu$ m pitch, but in this case, the output of the set-up has been connected to a multimeter to detect the output DC voltage. A -30dBm input power signal is applied to obtain an adequate response (value recommended in the datasheet). From the Fig. 39, it can be seen that this detector is more sensitive in the range 85-95GHz, obtaining higher values of output voltage.

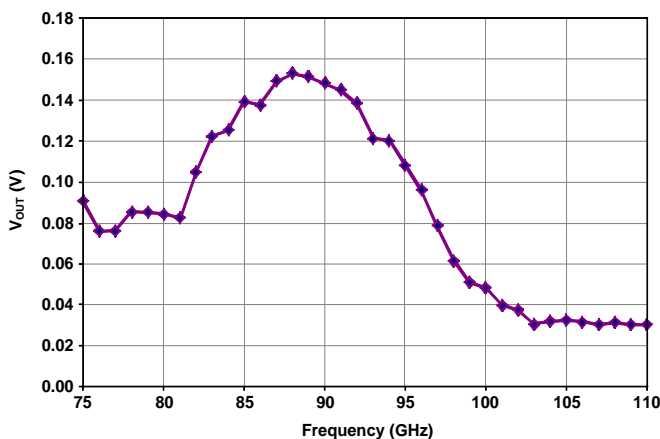


Fig. 39.Output voltage (V) of the V1A for a frequency sweep at a fixed input power

An on-wafer total power radiometer was formed by connecting the 4-stage LNA MMIC with the detector MMIC using wire bonding. RF input pad of the LNA and DC output pad of detector were left unconnected, to place the probes on them (Fig. 40 and Fig. 41).

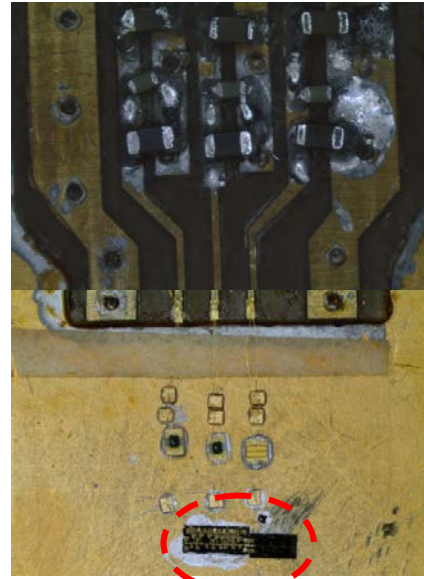


Fig. 40.On wafer assembly of the total power radiometer (LN4-110+V1A)

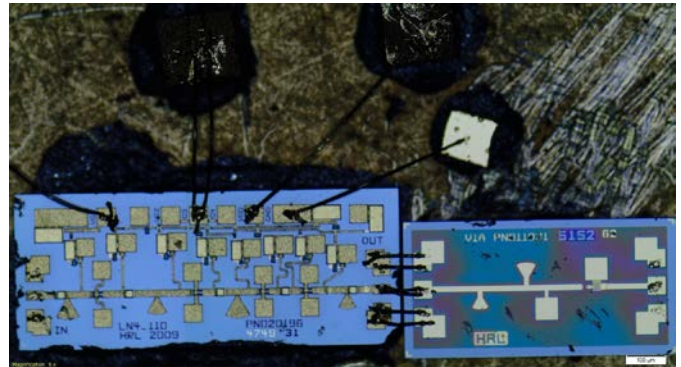


Fig. 41.Zoom of the total power radiometer assembly

Taking into account that the input power level in the detector is -30dBm and that the LN4-110 gain is about 20dB, the input power level of the total power radiometer should be a value of approximately -50dBm. The results obtained are shown in Fig. 42, where we can see a response similar to the single detector assembly.

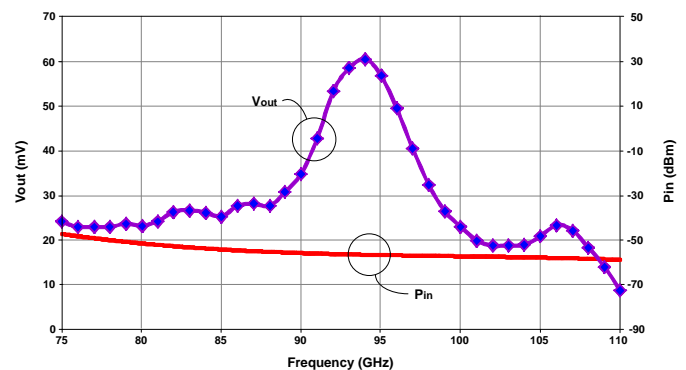


Fig. 42.Output voltage (mV) of the LN4-110+V1A for a frequency sweep and input power (dBm)

Now we are in process of preparing the on wafer assembly of the Medium power amplifier (LSPA2) in order to measure and characterize it.

## VI. DEVELOPMENT OF SPECIFIC MECHANICAL STRUCTURES AND MICROSTRIP HYBRID BOARDS FOR ASSEMBLING OF SYSTEMS

All of the partners had previous experience and background in developments reaching the high part of the microwave spectra (Q, V, etc.) but, for most of them, TeraSense meant a challenge for a further jump to W and G band. This increase in frequency means a decrease in size, therefore pushing the manufacturing facilities to the limits of accuracy and precision.

Lowest losses in the connection of system parts are provided by waveguides, compared to coaxial cables, but on the other hand a microstrip line environment seems more suitable for assembling MMICs and hybrids circuits. Therefore the development of waveguide-to-microstrip transitions becomes a primary requirement (section A). For some applications, like characterization of dielectric materials, quasi-optical configurations avoiding connectivity restrictions may be used. In section B a Quasi-optical Measurement System in W band for characterization of materials is presented. In section C an 80GHz Medium power amplifier assembling in WR10 waveguide is shown. Section D shows the design and measurements of a band pass filter in W band. In section E a study about optimum feasible coplanar to microstrip transitions is presented. Finally in section F the design of a WR10 waveguide Assembling of LNA in W band is shown.

### A. W-Band E-Plane Waveguide-to-Microstrip Transitions

This task has been developed by UNICAN. Regarding the robustness of the prototype, longitudinal E-plane transitions seem more suitable than other type of transitions to obtain the maximum transmitted signal. The waveguide-to-microstrip transition is composed of a standard W-band waveguide, WR-10, and a cut-off cavity which contains the required microstrip line and the strip transition entering the waveguide. This microstrip section is composed of the probe which captures the signal from the input WR-10 waveguide, a section of high-impedance microstrip line to compensate the impedance value for the capacitive reactance that the probe introduces, a quarter-wave impedance transformer to transform the impedance obtained at the end of this high-impedance line to the desired  $50 \Omega$  level and finally, a section of  $50 \Omega$  microstrip line.

Two of these structures have been optimized and connected to constitute a back-to-back transition necessary to measure the available circuits in the laboratory.

A thin substrate thickness is essential in W band to avoid unwanted propagation modes. A value of 5 mils or even lower thickness is considered suitable. A trade-off between low cost, flexibility, size and performance was required. Two versions, with RT/Duroid 5880 and with ULTRALAM 2000 have been used for the design and fabrication of the circuits.

#### A.1 RT/Duroid 5880 Substrate

This substrate is used for the waveguide-to-microstrip transition necessary for assembling of the available commercial MMICs. It has the following characteristics:  $h = 5$  mils,  $\epsilon_r = 2.2$  and  $\tan\delta = 0.0009 @ 10\text{GHz}$ . The design of the back-to-back transition can be seen in detail in [25],[26] and it is shown in Fig. 43.

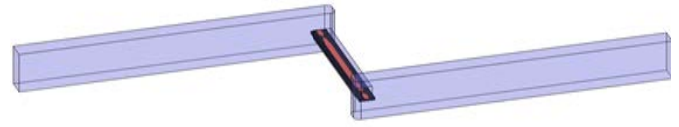


Fig. 43. The Back-to-Back Transition in W Band

The accuracy of the fabrication process is crucial for obtaining good experimental results. Several prototypes of the transition have been fabricated and measured with a high-resolution microscope, and the most similar to the nominal dimensions of the design has been selected. Furthermore, a good tolerance ( $\pm 20\mu\text{m}$  in the dimensions according to the manufacturer) was required too for the brass mechanized box (Fig. 44).



Fig. 44. Photographs of the Metal Case for the Back-to-Back Transition ( $4 \times 3 \times 2.4 \text{ cm}^3$ )

Finally, assembly of the microstrip lines on the metal case was done, as is depicted in Fig. 45. To attach the microstrip lines to the structure we have used solder and it has been necessary to be careful with the positioning of the microstrip lines into the cut-off cavity.

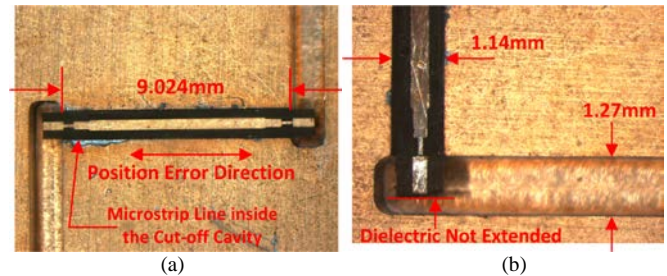


Fig. 45. The Final Assembly (Microstrip Lines inside the Metal Case). (a) View of the complete microstrip section. (b) Detail

The simulated S-parameters results are compared with respect to the obtained experimental measurements and they are shown in Fig. 46.

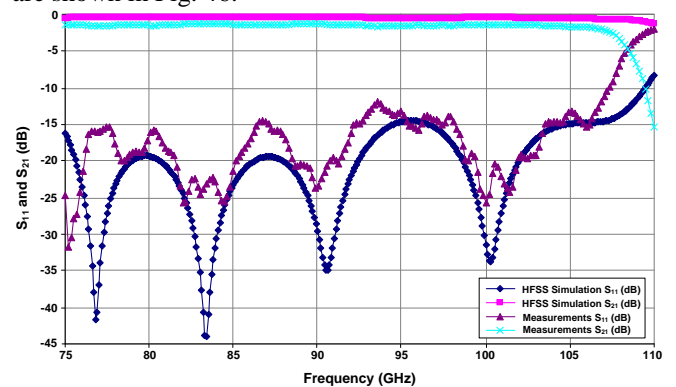


Fig. 46. A comparison between the measurements obtained and the previous simulation

Actual deviations from nominal dimensions in microstrip lines, displacement in their positioning and the effect of the gilding process of the microstrip line were included into the 3D EM simulator. This simulation reproduces more accurately the fabricated transition. Comparison with the measurements is shown in the Fig. 47, concluding that the agreement between measurements and simulation has improved. Differences between simulated and measured  $S_{21}$  may be related to the metal losses.

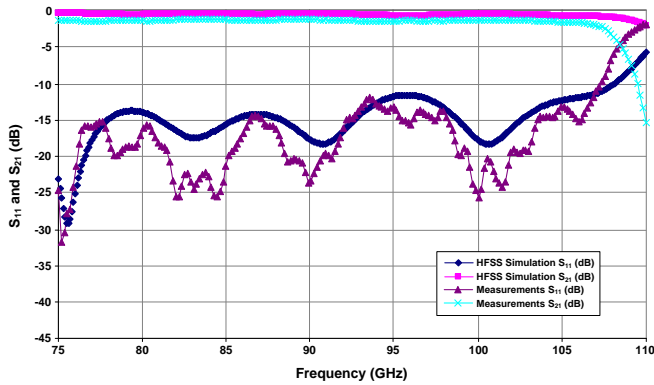


Fig. 47. A comparison between measurements and a more realistic simulation taking into account fabricated dimensions

#### A.2 Ultralam 2000 Substrate

This substrate, as it was said in subsection II.A, has been chosen for the design of the linear array of planar antennas feed by slots [11]. ULTRALAM 2000 has the next characteristics:  $h = 4\text{mils}$ ,  $\epsilon_r = 2.5$  and  $\tan\delta = 0.0019$ . The steps carried out during this design are identical to the previous transition and the comparison between simulated S-parameters and the measurements obtained in the laboratory can be seen in Fig. 48.

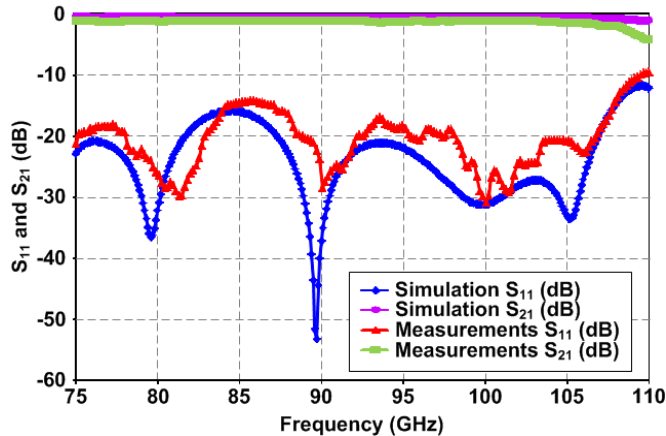


Fig. 48. Simulation and experimental results of the back-to-back transition in W-band

A double waveguide-to-microstrip transition (back-to-back transition) has been fabricated to check the validity of the design, although in the design of the array is only necessary a single transition.

#### B. W-Band Quasi-Optical Measurement System

The accurate knowledge of the properties of dielectric materials, such as those used to manufacture substrates, radomes, or lens antennas, is essential to carry out the design

of devices and circuits in the millimeter wave (MMW) range. The knowledge of the material properties can also be used in MMW scene simulators that render photorealistic images that allow one to predict if certain objects (i.e. metals, explosives...) can be identified within a scene for a given atmospheric effects, noise, blur or imaging system parameters [27],[28]. This task has been developed by UAB.

In the W-band (75 – 110 GHz), a quasi-optical measurement system [29] is an attractive alternative to measure these properties since it is contactless, non-destructive and the sample preparation is easy. Furthermore, broadband characterization can be achieved.

##### B.1 Measurement System Description

The designed measurement system is shown in Fig. 49. It consists of an input beam waist at the aperture of a feed horn that is refocused or collimated by an off-axis parabolic mirror to form an output beam waist at the sample position. The transmitted beam is passed, via another off-axis parabolic mirror to a second horn that feeds the receiver.

Unlike [29], we use reflective focusing elements instead of lenses. Reflective focusing elements are free from the absorptive and reflective losses that characterize refractive focusing elements. In order to keep cross-polarized radiation and distortion low it is convenient to have an effective focal length ( $f$ ) larger than the aperture diameter ( $D_a$ ) [30]. Therefore, we choose a commercial mirror of Janostech [31] with  $f = 152\text{ mm}$  and  $D_a = 101.6\text{ mm}$ .

A smooth-walled spline-profile horn [32] has been used as an alternative to a corrugated horn. The length of this horn (70 mm) is somewhat larger than a corrugated horn (40 mm) but it provides similar results with significant improvements in ease of manufacture.

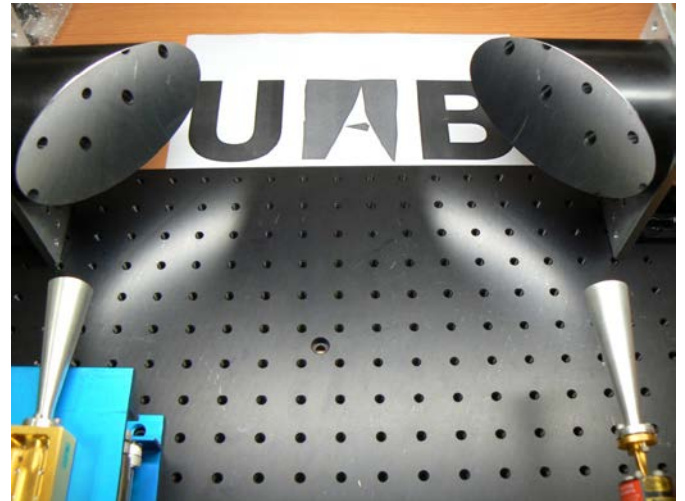


Fig. 49. Quasi-optical measurement system

##### B.2 Simulations and Experimental Validation

The proposed quasi-optical system through was validated through simulations using the physical optics (PO) implementation of FEKO [33].

In Fig. 50 we have depicted the near field in the plane defined by wave propagation. Indeed the input beam waist at the aperture of the feed horn is refocused at the sample while the radiation is largely collimated, thus keeping spill-over losses low.

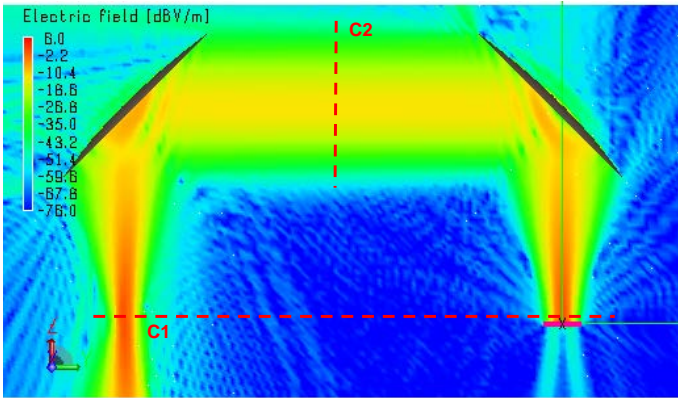


Fig. 50. Near field generated by the proposed quasi-optical measurement system at 94 GHz

The near field along the cut C1 is plotted in Fig. 51. It can be seen that input gaussian beam is recovered without appreciable losses. The computed gaussianity of the beam at C2 is 99.5% thus we can assume that a plane wave is obtained at the sample plane as predicted.

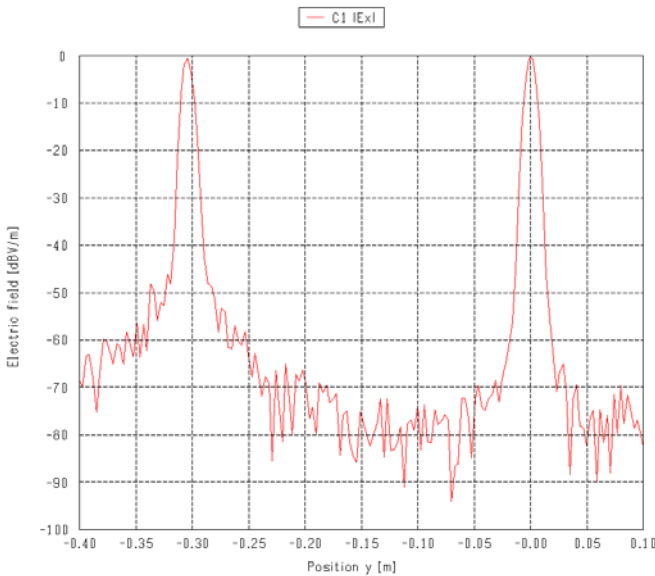


Fig. 51. Near field along C1. The input gaussian beam is recovered without noticeable losses

The measured system efficiency is around 80% in the entire W-band. This efficiency includes losses in the free space path, horns and waveguide transitions.

The proposed setup has also been used in order to characterize a homemade teflon lens. Measurements and simulations (Fig. 52) show an excellent agreement.

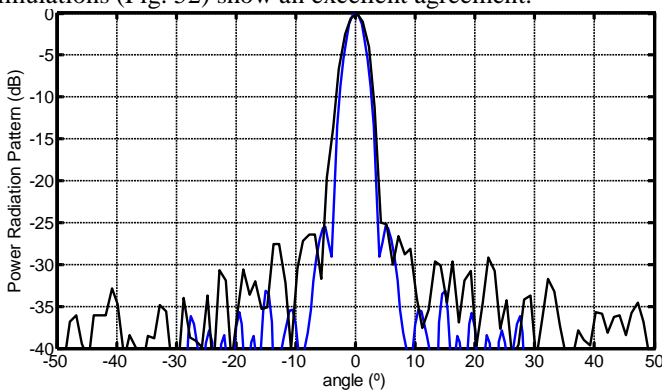


Fig. 52. Characterization of a zone plate lens

### C. 80 GHz Medium Power amplifier

This task has been developed by UPC. An 80 GHz medium power amplifier MMIC Hittite AUH-320 has been mounted using two finline waveguide to microstrip transitions. The components have been placed on a brass mechanized box where both the input and the output of the box are WR-10 waveguides. Fig. 53 shows the finline transition placed on the channel of one half of the box.

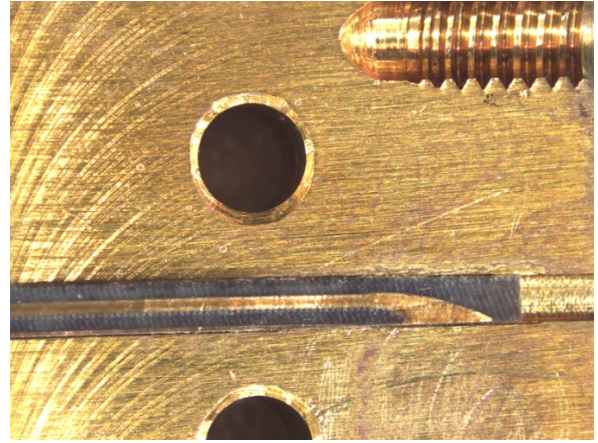


Fig. 53. Finline transition placed on half of the WR-10 waveguide

The MMIC has been fixed to the box channel using conductive epoxy to have a ground contact with the box. The connections to the finline transitions and to the DC bias have been performed using thermo-compression wire bonding. Fig. 54 shows a photograph of the MMIC placed on the box channel. The upper part of the image shows the bias circuitry connected to the MMIC by wire bonding.



Fig. 54. Amplifier MMIC placed on the box. Both finline transitions as well as the DC biasing are connected by wire bonding

The amplifier gain and return loss have been measured from 74 GHz to 86 GHz. Fig. 55 shows the measured gain of the amplifier. A maximum gain of 16 dB is obtained at 78 GHz, agreeing with the specifications provided by the manufacturer. Additionally, Fig. 56 shows the measured return loss of the amplifier showing a good matching from 78 GHz to 83 GHz.

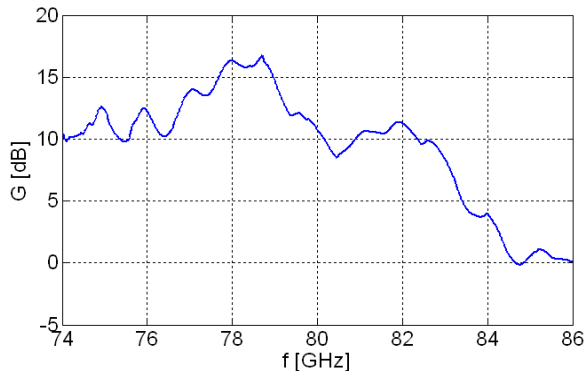


Fig. 55. Measured gain of the amplifier.

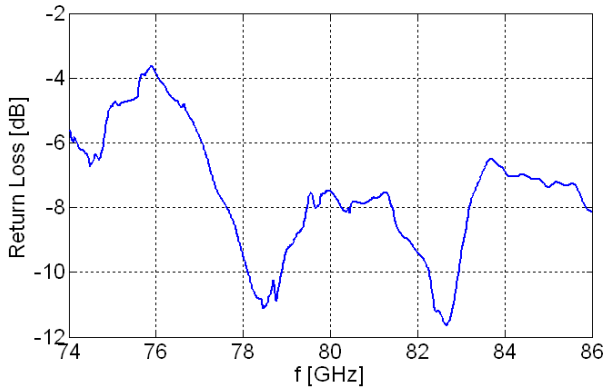


Fig. 56. Return loss of the amplifier

#### D. Band pass Filter

This task has been developed by UNICAN. Five-stages coupled microstrip band pass filters in W band have been designed and manufactured in 5 mils thickness substrate (RT/Duroid 5880). The objective of this filter is to define the 6 GHz-bandwidth (from 94GHz up to 100GHz) shape of a total power radiometer design.

This band pass filter is connected with the same model of coplanar-to-microstrip transitions (model PROBE POINT TM0503 transition) used in diode characterization [18], and bonded with gold wires with a diameter of  $17\mu\text{m}$  in order to enable on-wafer measurements using air coplanar probes. The complete assembly fixed with conductive epoxy can be seen in Fig. 57.

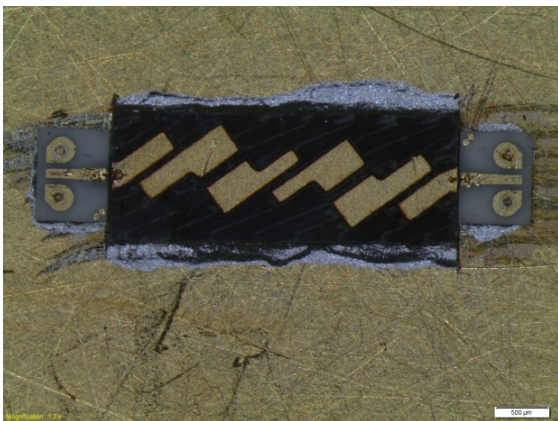


Fig. 57. Assembly of the band pass filter in W-band

Comparing simulation results and on-wafer experimental measurements (see Fig. 58), around 6dB of difference in losses ( $S_{21}$  parameter) can be seen. This may be due to the coplanar-to-microstrip transitions and gold wires losses. A more similar matching has been obtained ( $S_{11}$  parameter).

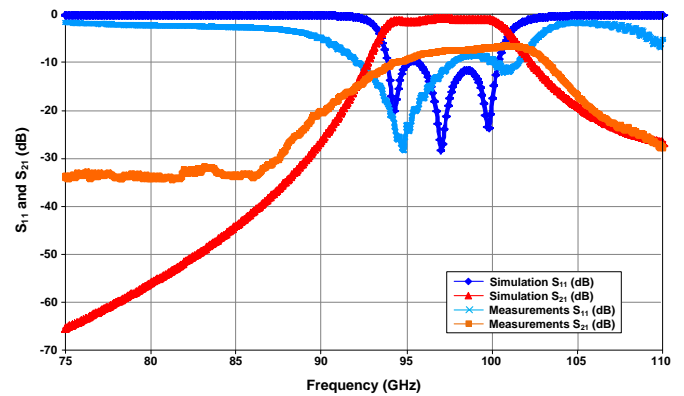


Fig. 58. Simulation and experimental results of the band pass filter in W-band

Finally, the use of this filter has been discarded in the assembly of the total power radiometer in order to maximize the bandwidth and sensitivity of the own radiometer. This decision was taken from the comparison of several simulations of the complete system radiometer [34],[24].

#### E. Coplanar-to-Microstrip Transitions Study

This task has been developed by UNICAN. Flip chip mounting is preferred (i.e. for diodes), but if wire bonds are unavoidable, (MMICs) coplanar-to-microstrip transitions should be carefully designed to minimized mismatching and degradation of on-wafer response. Those reasons drove us to a comparative study with simulations and measurements of different transitions affordable by our manufacturing facilities.

The assembly of MMICs in a metal case housing needs the waveguide-to-microstrip transitions previously shown in subsection IV.A, both for input and output. The own termination of this transition uses microstrip technology and the MMICs presents coplanar inputs and outputs, therefore coplanar-to-microstrip transitions are necessary in the assembly.

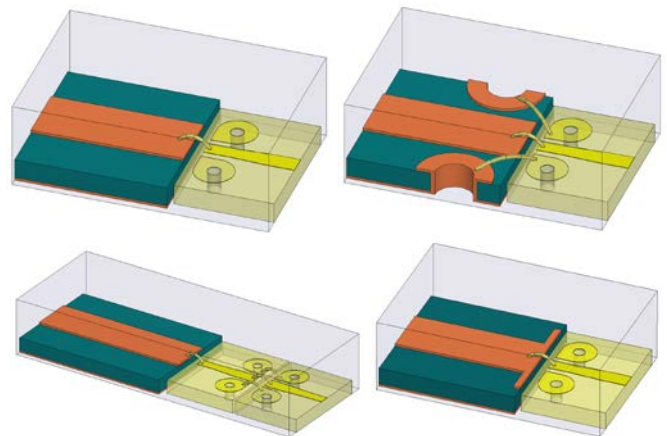


Fig. 59. Different options for the monolithics connections

A coplanar-to-microstrip transition (model PROBE POINT TM0503 transition) has been used in the simulation instead of the MMIC coplanar input since it presents coplanar technology. In four configurations simulated (see Fig. 59) [24], the common part in the design is a 50 Ohm microstrip line as input and the coplanar-to-microstrip transition as output, which are connected with gold wire bonds. All aspects are taking into account to obtain a more realistic result analyzing possible mismatching and losses due to these connections. The comparison is done in terms of S-parameters.

The four configurations are different in the following characteristics:

- Top left image (Config.1): the connection has made with a single wire bond between both parts.
- Top right image (Config. 2): home-made via-holes have been used in this case in the microstrip part with one wire bond for the central conductor line and one wire bond for each ground.
- Bottom left image (Config. 3): use another coplanar-to-microstrip transition in the middle in order to join both parts, placing microstrip parts in the same side and coplanar parts joined with wires bond (central conductor line and two grounds) too.
- Bottom right image (Config. 4): the connection is made with a single wire bond and furthermore including a wider section line following the 50 Ohm microstrip line to compensate the wire bond inductive effect.

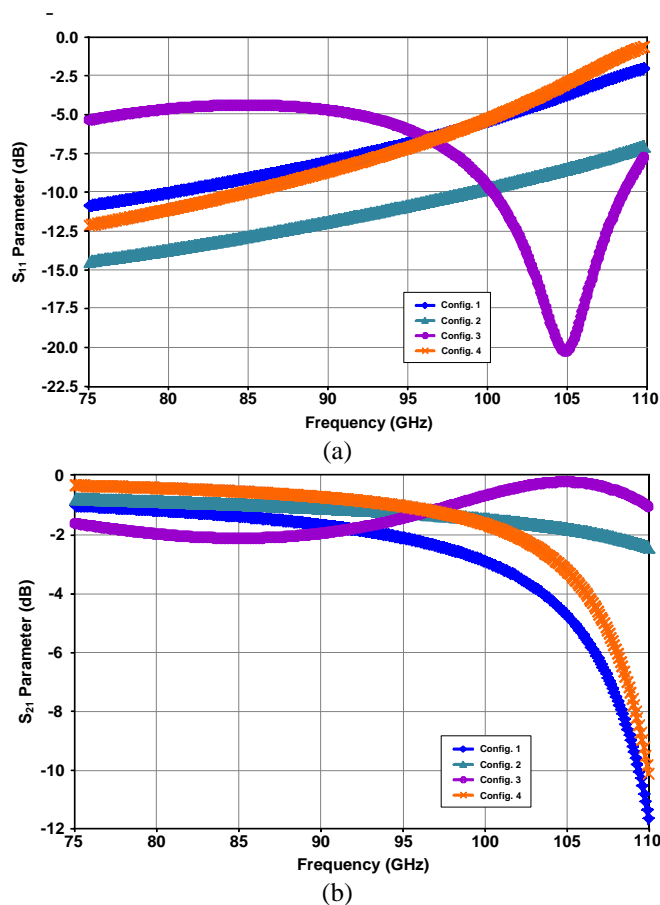


Fig. 60. Electromagnetic Simulation Results of 4 Configurations (a)  $S_{11}$  Parameter, (b)  $S_{21}$  Parameter

From the results obtained shown in Fig. 60, Configuration 2 (including home-made via-holes in microstrip part) would be the best option especially considering the losses in comparison with others configurations, obtaining an acceptable matching in the entire band too.

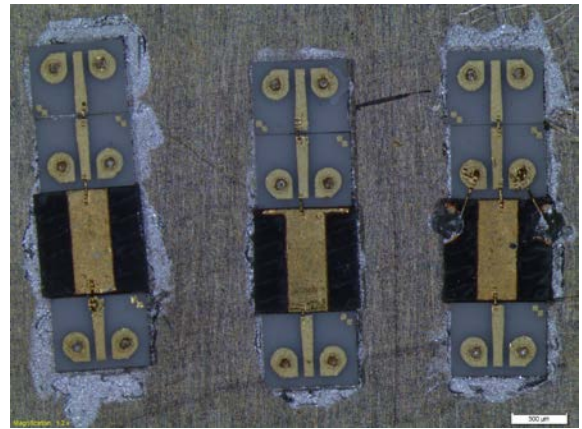


Fig. 61. Different options for the monolithics connections

The fabricated prototypes can be seen in Fig. 61. Configuration 3 has not been fabricated due to its complexity for using another coplanar-to-microstrip transition. Two additional transitions have been necessary in input/output to place the air coplanar probes.

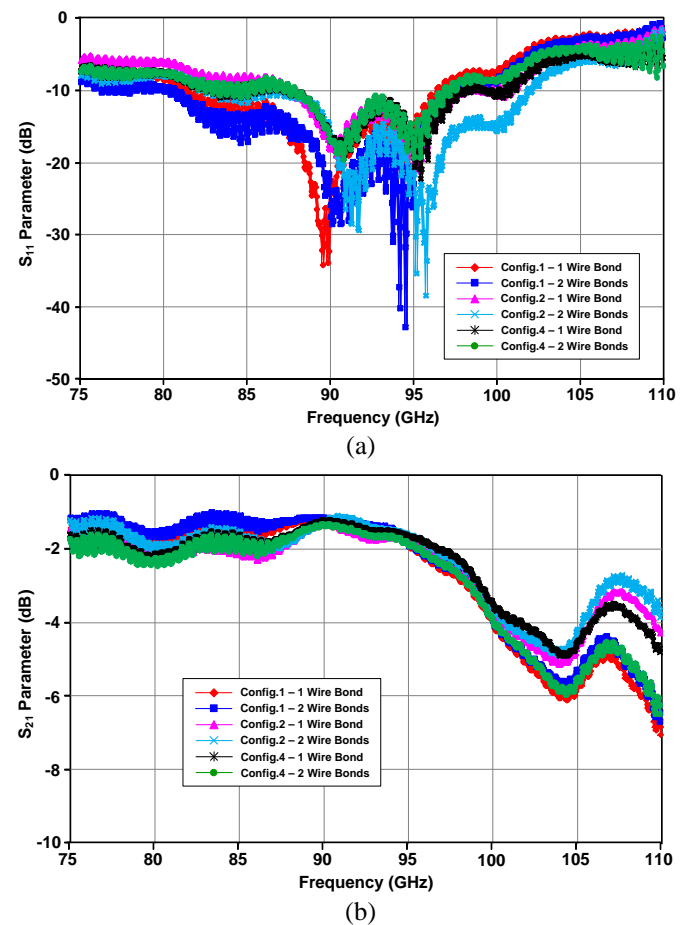


Fig. 62. Measurements Results of 3 Configurations with one or two wire bonds between external coplanar-to-microstrip transitions and input/output of the circuits (a)  $S_{11}$  Parameter, (b)  $S_{21}$  Parameter

From the comparison between the results obtained from the on wafer measurements (shown in Fig. 62) of the 3 configurations and one or two wire bonds in external connections for each configuration, it can be concluded that Configuration 2 (with home-made via-holes to hold as much as possible the coplanar filed structure) with one or two wire bonds is the best solution to match the system.

#### F. WR-10 waveguide Assembling of LNA in W band

This task has been developed by UNICAN. The general purpose transition previously presented was adapted to be used in a case housing a single LNA and in another case housing an LNA plus a detector to constitute a total power radiometer.

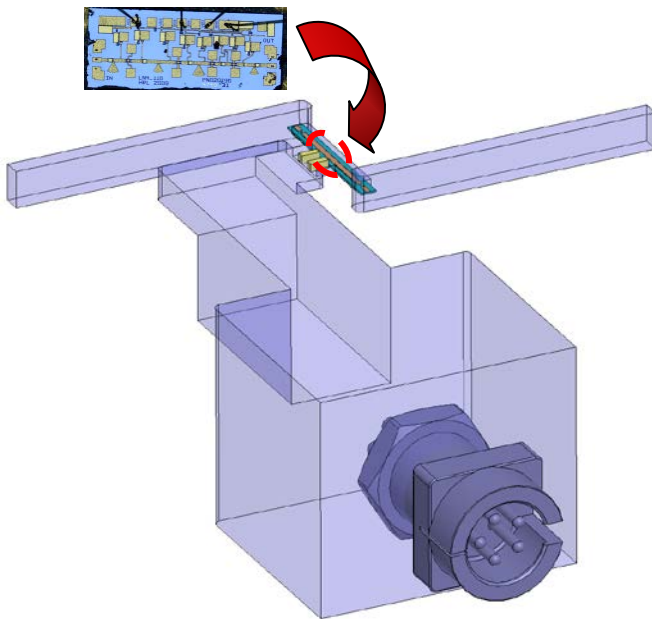


Fig. 63. Redesign of the back-to-back transition to measure LN4-110 in a case housing

For the design of the housing case, we start from the design of the back-to-back transition previously shown in subsection VI.A1. Previous simulation has been presented in [24]. This transition has been modified adding in the middle of the cut-off cavity an aperture to include the DC bias elements (resistances and capacitors) for the transistors which form the LNA MMIC. The cavity has been split into three narrow channels (suitable width for assembly of DC components) to avoid possible resonances in the cut-off cavity and its size has been increased in steps to host the DC connector as it can be seen in Fig. 63.

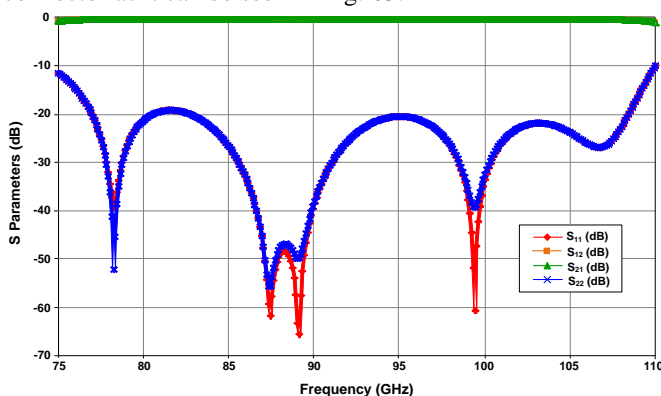


Fig. 64. S Parameters of the transition simulation

The results obtained in the simulation are presented in Fig. 64, where we can see similar results of the back-to-back transition and a good matching in the entire band.

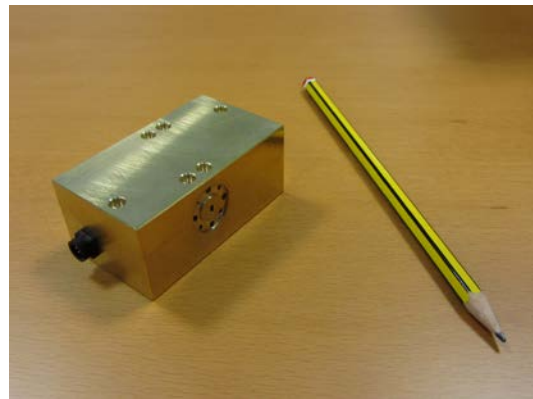


Fig. 65. Metal case of the back-to-back transition for LN4-110 ( $7 \times 4 \times 3 \text{ cm}^3$ )

The transition was fabricated by the same manufacturer that the back-to-back transition. The metal case, which can see in Fig. 65, is formed by two pieces split with the same technical concept. These details are shown in Fig. 66. Moreover, we can observe the connector which is used to DC bias the LN4-110.

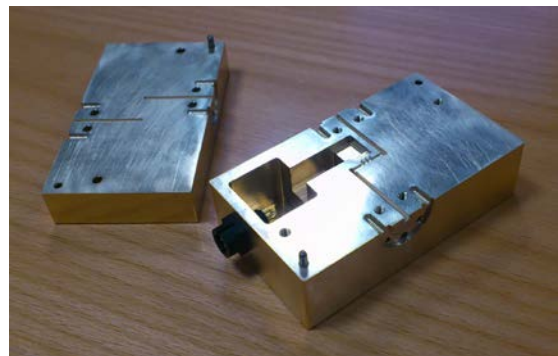


Fig. 66. Details of the metal case which is split into two pieces

Furthermore, the microstrip line sections which form each of the transitions have been fabricated (see Fig. 67) with the previous configuration chosen: the home-made via-holes to be connected with the input/output of the LN4, maintaining the coplanar field structure and providing the minimum mismatching in this part of the assembly.

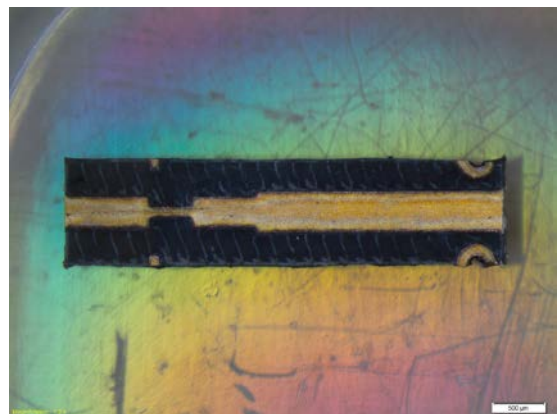


Fig. 67. A single transition with home-made vias for assembly of the LN4-110 into the metal case

Finally, the following step is to assemble the complete circuit with the LN4-110, the single transitions with the home-made via-holes, the DC components (resistances and capacitors), substrates where the components will be placed, the DC connector and the wire bond necessary to join each component. A detail can be seen in Fig. 68.

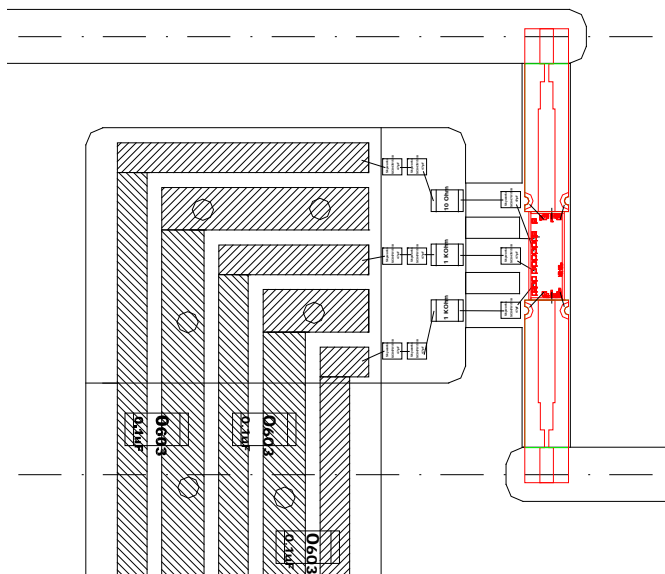


Fig. 68. Detail of the assembly of the LNA4-110 into the metal case with all necessary components

## VII. MMW IMAGES IN BIOMETRIC APPLICATIONS

This section describes the application of MMW images in the field of biometric recognition. This task has been developed by UAM. Biometric recognition is the science which studies the recognition of humans through one or several physiological and/or behavioral characteristics [35]. Many biometric characteristics are used to identify individuals: fingerprint, signature, iris, voice, face, hand, etc. Biometric traits such as the ear, face, hand and gait are usually acquired with cameras working at visible frequencies of the electromagnetic spectrum. Such images are affected by, among other factors, lighting conditions and the body occlusion (e.g., clothing, make up, hair, etc.). In order to circumvent these limitations, researchers have proposed the use of images acquired at others spectral ranges: X-ray, infrared, millimeter (MMW) and submillimeter (SMW) waves [36]. The images captured beyond the visible spectrum overcome, to some extent, some of the mentioned limitations; furthermore, they are more robust to spoofing than other biometric images/traits. Among the spectral bands out of the visible spectrum, the millimeter waves (with frequency in the band of 30-300 GHz) present interesting properties that can be exploited in biometrics (see Fig. 69): ability to pass through cloth and other occlusions, innocuous to health, low intrusiveness, and the recent deployment and rapid progress of GHz-THz systems in screening applications. However, the usage of this kind of data in biometrics has not received much attention [37],[38], mainly due to the lack of available databases of MMW images. This is a consequence of: (i) the privacy concern these images present, and (ii) most of the imaging systems working at the MMW/SMW band are either in prototype form or not easily accessible for research.

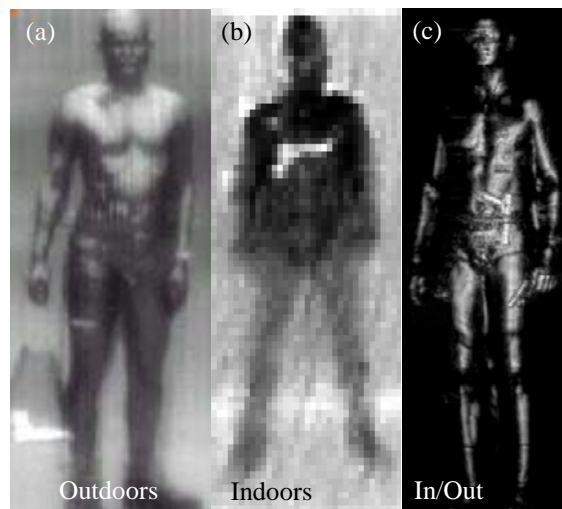


Fig. 69. Examples of MMW body images for active/passive systems in outdoors and indoors scenarios, taken from [36]

We describe briefly the development of a biometric system using synthetic MMW body images. First, a database of synthetic MMW images, BIOGIGA [39], was collected from 50 people (25 males and 25 females). This database contains images simulating passive and active systems in indoors and outdoors scenarios. Only the data corresponding to a passive system in outdoors scenarios was considered.

The features extracted from the body images were based on geometrical measures between the different parts of the body silhouette. First the input image is segmented from the background and the body silhouette is extracted. Also a basic skeleton of the body is obtained through morphological operations, and six reference points. A large set of body landmarks is obtained calculating the Euclidean distance between each reference point and the body contour, and analyzing maxima and minima values. Finally, a set of 21 measures between different landmarks is obtained, which forms the feature vector used in the recognition stage of the system. Apart from this set of measures, a feature selection algorithm SFFS (Sequential Floating Forward Selection) was also used to find the most discriminative set of distance-based features. Fig. 70 shows some images of the stages of the feature extraction process.

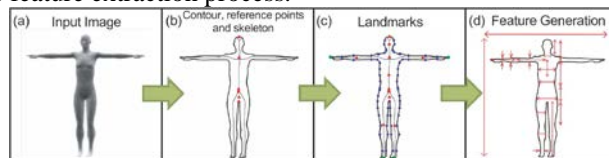


Fig. 70. Feature extraction process. (a) Input image corresponding to MMW passive system in outdoor scenario. (b) Contour, reference points and skeleton. (c) Landmark extraction. (d) Set of distances measured which form the feature vector

Table 4 shows the experimental results obtained for the biometric system developed. Three experimental protocols were used: 1:3, 2:3 and 3:3, the first number indicating the number of images used for model training and the second number indicating the number of images used for testing. Results are given in the form of equal error rate (EER), which is a popular measure in the pattern recognition community. Results of 2% EER were obtained for the three protocols when using the 21 features extracted. These results were improved significantly when the SFFS feature selection

algorithm was used, obtaining 0.08% EER for the 1:3 protocol and 0% EER, i.e., no errors were found for the other two protocols.

Protocol	Using all features	Using SFFS feature selection	
	EER (%)	# of feat. selected	EER (%)
1:3	2.0	6	0.08
2:3	2.0	4	0.0
3:3	2.0	3	0.0

Table 4. Results in terms of EER of the biometric system using MMW body images

### VIII. CONCLUSIONES

The CSD2008-00068 TERASENSE CONSOLIDER project permitted the extension upwards in frequency of the previous background of the microwaves research group partners. This article compiles some of the technology developments in the frame of the TERASENSE work package “THz Device Technology Laboratory”, particularly in aspects like antenna manufacturing, characterization of active and passive devices, design and assembling of circuits and data processing. An initial great jump has been done, which, if the activities in these THz bands continue in the future, may allow settling a solid background for development of new applications.

### ACKNOWLEDGEMENTS

This work was supported by the Spanish Ministerio de Ciencia e Innovación through the CONSOLIDER-INGENIO 2010 program reference CSD2008-00068 TERASENSE.

### REFERENCIAS

- [1] Siegel, P.H. Terahertz Technology. IEEE Transactions on Microwave Theory And Techniques, Vol. 50, No. 3. March 2002
- [2] Räisänen, A.V. Challenges of Terahertz. The Second European Conference on Antennas and Propagation, EuCAP 2007. 2007
- [3] Oka, S.; Togo, H.; Kukutsu, N.; Nagatsuma, T. “Latest Trends in Millimeter-Wave Imaging Technology”. Progress In Electromagnetics Research Letters, Vol. 1, 197–204, 2008
- [4] Shur, M. Terahertz technology: devices and applications. Proceedings of ESSCIRC, Grenoble, France. 2005
- [5] S. Yeom, D.-S. Lee, H. Lee, J.-Y. Son, V.P. Guschin, “Distance Estimation of Concealed Objects with Stereoscopic Passive Millimeter-Wave Imaging”, Progress in Electromagnetics Research Letters, Vol. 115, 399-407, 2011
- [6] P.H. Siegel and R.J. Dengler, “Terahertz Heterodyne Imaging: Introduction and Techniques,” Int. Journal of Infrared and Millimeter Waves, v.27, no. 4, April 2006.
- [7] Essen, H.; Fuchs, H.; Hägelen, M. [et al.]. Concealed Weapon Detection with Active and Passive Millimeterwave Sensors, Two Approaches. [http://duepublico.uni-duisburg-essen.de/servlets/DocumentServlet/Document/14694/Final\\_Papers/GM0004-F.pdf](http://duepublico.uni-duisburg-essen.de/servlets/DocumentServlet/Document/14694/Final_Papers/GM0004-F.pdf)
- [8] Stanko, S.; Nötzel, D.; WAHLEN, A.; [et al.]. 2008. Active and Passive mm-Wave imaging for Concealed Weapon Detection and Surveillance. 33rd International Conference on Infrared, Millimeter and Terahertz Waves, IRMMW-THz 2008
- [9] Tessmann, A.; Kudszus, S.; Feltgen, T.; [et al.]. 2002. Compact single-chip Wband FMCW radar modules for commercial high resolutions sensor applications. IEEE Transactions on Microwave Theory and Techniques, Vol. 50, Issue 12
- [10] Sato, M.; Sato, H.; Hirose, T.; [et al.]. 2007. Compact receiver module for a 94GHz band passive millimeter-wave imager. In Special Issue on Asia Pacific Microwave Conference 2007
- [11] N. Amar, J. Gutiérrez, A. Tazón, F. Cátedra, A. Mediavilla. “Array Lineal de Antenas planas Excitadas por Ranuras en la Banda W”. XXVII Simposium Nacional de la Unión Científica Internacional de Radio (URSI 2012). 12-14 Septiembre. Elche. (ISBN 9788469543269)
- [12] O. Fernández, A. Gómez, J. Gutiérrez, A. Tazón, A. Vegas. “Enhancement of the radiation properties of a lineal array of planar antennas with a chiral metamaterial cover”. 9th Spanish Conference on Electron Devices. Palacio de Congresos Conde Ansúrez. Valladolid. Febrero 2013
- [13] Nova, E.; Rodrigo, D.; Romeu, J. & Jofre, L., “94 GHz cassegrain reflector antenna performance characterization”, Antennas and Propagation (EUCAP), 2012 6th European Conference on, 2012, 3442 - 3445.
- [14] A.G.Pino, N.LLombart, B.Gonzalez-Valdes and O. Rubiños; “A Bifocal Ellipsoidal Gregorian Reflector System for THz Imaging Applications,” IEEE Transactions on Antennas and Propagation, vol. 60, no. 9, pp. 4119–4129, Sep. 2012.
- [15] J. Montero-de-Paz, I. Oprea, V. Rymanov, S. Babiél, E. García-Muñoz, A. Lisauskas, M. Hoefle, Á. Jimenez, O. Cojocari, D. Segovia-Vargas, M. Palandöken, T. Tekin, A. Stöhr, and G. Carpintero, "Compact Modules for Wireless Communication Systems in the E-Band (71–76 GHz)", Journal of Infrared, Millimeter, and Terahertz Waves, vol. 34, Issue 3-4, pp 251-266, April 2013.
- [16] J. Montero-de-Paz, E. Ugarte-Muñoz, M. Hoefle, I. Oprea, A. Lisauskas, O. Cojocari, L.E. García-Muñoz, D. Segovia-Vargas, G. Carpintero, "Antenna Effect on the Responsivity of Schottky Diode Receivers in the E-Band", IEEE Transactions on Antennas and Propagation, submitted.
- [17] J. Montero-de-Paz, E. Ugarte-Muñoz, L.E. Garcia-Muñoz, D. Segovia-Vargas, D. Schoenher, I. Oprea, A. Amrhein, O. Cojocari, H.L. Hartnagel, "Millimeter-wave receiver based on a folded dipole antenna and Schottky diode for maximum power transfer", (2012) Proceedings of 6th European Conference on Antennas and Propagation, EuCAP 2012, art. no. 6206286, pp. 1259-1262, 26-30 March, Prague, Czech Republic.
- [18] K. Zeljami, J. Gutiérrez, J. P. Pascual, T. Fernández, A. Tazón, M. Boussouis. “Characterization and modeling of Schottky diodes up to 110GHz for use in both flip-Chip and wire-bonded assembled environments”. Progress In Electromagnetics Research, Vol. 131, pp.457-475, 2012
- [19] K. Zeljami, T. Fernández, J.P. Pascual, A. Tazón, M. Boussouis, “Modelado de Diodos Schottky para Aplicaciones a Frecuencias de Terahercios”. XXV Symposium Nacional de la Unión Científica Internacional de Radio (URSI-2010). 14-16 Septiembre. Bilbao
- [20] K. Zeljami, J. Gutiérrez, J.P. Pascual, T. Fernández, A. Tazón. “Caracterización de Transiciones Coplanar-Microstrip en Banda W”. XXVI Symposium Nacional de la Unión Científica Internacional de Radio (URSI-2011). 07-09 Septiembre. Leganés (ISBN: 978-84-933934-5-8)
- [21] K. Zeljami, J. Gutiérrez, J.P. Pascual, T. Fernández, A. Tazón, M. Boussouis. “Caracterización de Diodos Schottky para Banda W”. XXVII Symposium Nacional de la Unión Científica Internacional de Radio (URSI 2012). 12-14 Septiembre. Elche. (ISBN 9788469543269)
- [22] M. Arias, L. De La Fuente, J.P. Pascual, A. Tazón. “Amplificador Mhemt Cascodo de Bajo Ruido a 100 GHz”. XXIV Symposium Nacional de la Unión Científica Internacional de Radio (URSI-2009). 16-18 Septiembre. Santander (ISBN: 978-84-8102-550-7)
- [23] M. Arias, L. De La Fuente, J.P. Pascual, A. Tazón. “Diseño de un Amplificador MHEMT de Media Potencia a 94-100 GHz”. XXIV Symposium Nacional de la Unión Científica Internacional de Radio (URSI-2009). 16-18 Septiembre. Santander (ISBN: 978-84-8102-550-7)
- [24] J. Gutiérrez, K. Zeljami, T. Fernández, J.P. Pascual, A. Tazón. “Caracterización de Componentes y Balance de Potencia para Radiómetro en Banda W”. XXVII Symposium Nacional de la Unión Científica Internacional de Radio (URSI 2012). 12-14 Septiembre. Elche. (ISBN 9788469543269)
- [25] J. Gutiérrez, K. Zeljami, J.P. Pascual, T. Fernández, A. Tazón, A. Mediavilla, E.S. Pana. “Yield-Oriented Design Protocol and Equivalent Circuit Model for W-Band E-Plane Waveguide-to-Microstrip Transitions”. International Journal of RF and Microwave Computer-Aided Engineering. (2013) DOI: 10.1002/mmce.20716
- [26] J. Gutiérrez, K. Zeljami, T. Fernández, J.P. Pascual, A. Tazón, Á. Mediavilla, S. Pana. “Transición Guía de Onda-Microstrip en Banda W”. XXVI Symposium Nacional de la Unión Científica Internacional de Radio (URSI-2011). 07-09 Septiembre. Leganés (ISBN: 978-84-933934-5-8)
- [27] M.R. Fetterman, J. Grata, G. Jubic, W.L. Kiser, Jr., A. Visnansky, “Simulation, acquisition and analysis of passive millimeter-wave images in remote sensing applications”, Optics Express, vol. 16, nº. 25, pp. 20503–20515, Dec 2008.
- [28] E. L. Stein, Jr., C. A. Schuetz, R. D. Martin, J. P. Samluk, J. P. Wilson, D. G. Mackrides, J. A. Murakowski, M. Murakowski, D. W. Prather,

- “Passive Millimeter-Wave Cross Polarization Imaging and Phenomenology” Proc. of SPIE, vol. 7309, no. 730902, Apr. 2009. <http://dx.doi.org/10.1117/12.819033>
- [29] D. Bourreau, A. Péden, S. Le Maguer, “A Quasi-Optical Free-Space Measurement Setup Without Time-Domain Gating for Material Characterization in the W-Band,” IEEE Trans. on Instrumentation and Measurement, vol. 55, n° 6, pp. 2022-2028, Dec. 2006
- [30] P. F. Goldsmith, Quasioptical Systems, IEEE Press, 1998
- [31] [www.janostech.com](http://www.janostech.com)
- [32] C. Granet, G.L. James, R. Bolton, G. Moorey, “A Smooth-Walled Spline-Profile Horn as an Alternative to the Corrugated Horn for Wide Band Millimeter-Wave Applications”, IEEE Trans. on Antennas and Propagation, vol. 52, n°3, pp. 848-854, Mar. 2004.
- [33] [www.feko.info](http://www.feko.info)
- [34] J. Gutiérrez, J.P. Pascual, T. Fernández, P. De Paco, A. Tazón, J. Parrón, O. Menéndez. “Configuraciones Para Radiómetro De Potencia Total En Banda W”. XXV Symposium Nacional de la Unión Científica Internacional de Radio (URSI-2010). 14-16 Septiembre. Bilbao
- [35] A. Jain, A. Ross, and S. Prabhakar, “An Introduction to Biometric Recognition”, IEEE Trans. on CSVT. Vol. 14, No. 1, pp. 4-20, 2004.
- [36] M. Moreno-Moreno, J. Fierrez, and J. Ortega-Garcia, “Biometrics Beyond the Visible Spectrum: Imaging Technologies and Applications,” in Proceedings of BioID-Multicomm 2009, LNCS 5707, 154–161, Springer (September 2009).
- [37] B.G. Alefs, R.J.M. den Hollander, F.A. Nennie, E.H. van der Houwen, M. Bruijn, W. van der Mark, and J.C. Noordam, “Thorax biometrics from Millimetre-Wave images,” Pattern Recognition Letters 31(15), 2357–2363 (2010).
- [38] M. Moreno-Moreno, J. Fierrez, R. Vera-Rodriguez and J. Parron, “Simulation of Millimeter Wave Body Images and its Application to Biometric Recognition”, in Proc. International Conferencie SPIE, Defense Security and Sensing, SPIE, 2012.
- [39] M. Moreno-Moreno, J. Fierrez, P. Tome, R. Vera-Rodriguez, J. Parron and J. Ortega-Garcia, “BioGiga: Base de datos de imagenes sinteticas de personas a 94 GHz con fines biometricos”, in Proc. of XXVI Symposium Nacional de Union Científica Internacional de Radio, URSI 2011, Madrid, Spain, September 2011.